

Näide: kaose “mäng”

1. Kaose “mäng” kolmnurgas
2. Kaose “mäng” nelinurgas
3. DNA analüüs

Viiteid:

1. Peitgen H.-O., Jürgens H., Saupe D., Chaos and Fractals, Springer, New York et al., 1992.
2. Peak D., Frame M. Chaos under Control. Freeman, New York, 1994.

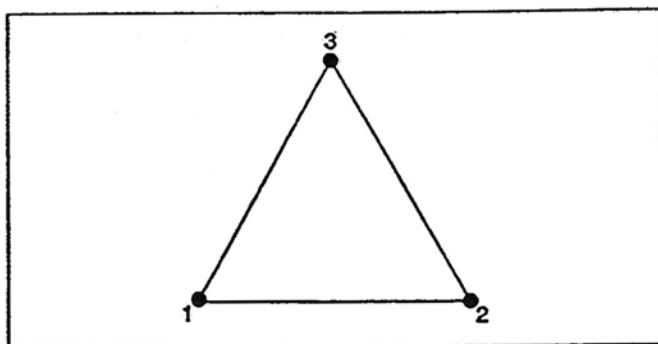


Figure 6.1 : The game board of our first chaos game.

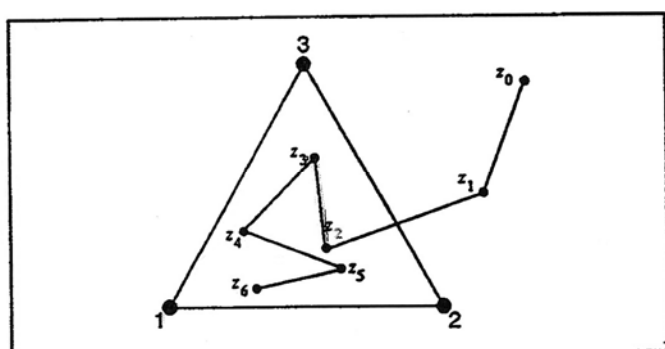


Figure 6.2 : The first six steps of the game. Game points are connected by line segments.

The First Steps ...

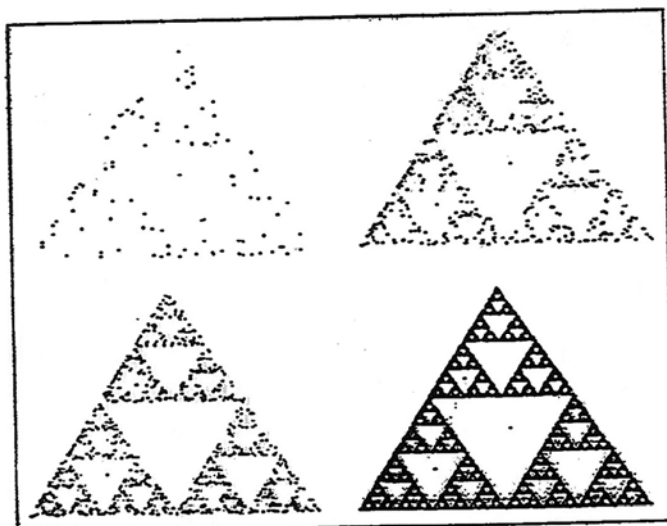


Figure 6.3 : The chaos game after 100 steps (a), 500 steps (b), 1000 steps (c), and 10 000 steps (d). Only the game points are drawn without connecting lines. (Note that there are a few spurious dots that are clearly not in the Sierpinski gasket.)

... and the Next Game Points

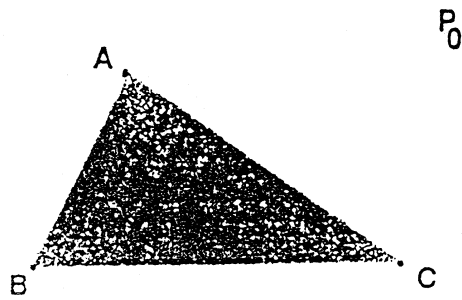
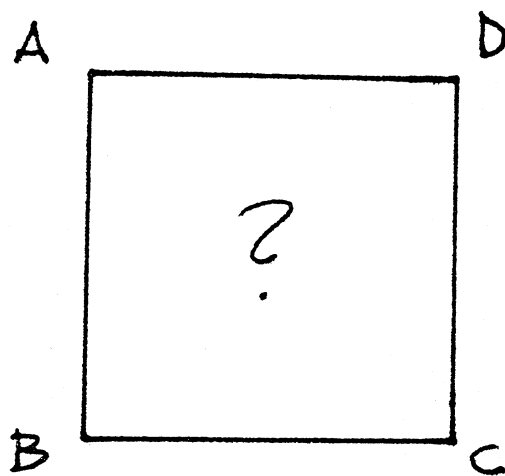


Figure 1.20 *The Chaos Game (Three Corners, Two-thirds Version).*



DNA is composed of four chemically different building blocks, called bases, which are designated by the letters A, C, G, and T. All biological information is thought to be encoded in “words” spelled from these letters. If we look at the string of A’s, C’s, G’s, and T’s making up a given gene (a piece of DNA encoding the rules for making a protein), it’s very hard for the untrained eye to see much rhyme or reason in it. Here’s an example, using the first 250 or so bases in the DNA coding for the enzyme amylase:

```
GAATTCAAGTTTGGTGCAAACTTGGCACAGTTATCCGCAAG
TGGAATGGAGAGAAGATGTCCTATTTAAAGTAAATATATACG
ATTTTGTCAATTTGTTCTGTCATACATCTGTTGTCAATTTCTTAA
ATATTGTAACCTTAAATTGTTGATTATTAGTTAGGCTTATTGTT
CATTTATCCTTAATTAATTATGTTTTTCATTTGATACATCAGT
CACCTGATAACAGCTGAAATCTAAAGTATCACTTAGTGAGTT
TTGTTGGGTTGTGTT
```

But if we make a square with corners labeled A, C, G, and T, take a starting point in the middle of the square, and then play the Chaos Game by going halfway to a previous point from the vertex whose letter appears next in a given DNA string (many such strings have been identified, in everything from primitive organisms to humans), some of the syntax of this code jumps out.

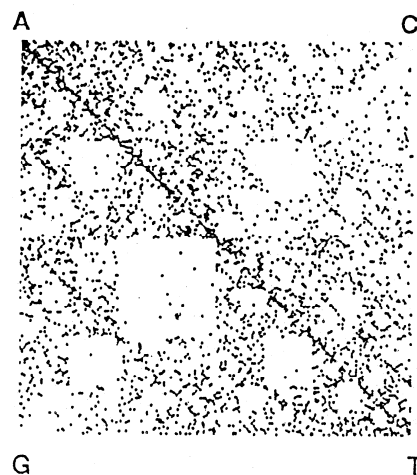


Figure 1.23 *Four-cornered Chaos Game picture generated by the DNA encoding the enzyme amylase.*

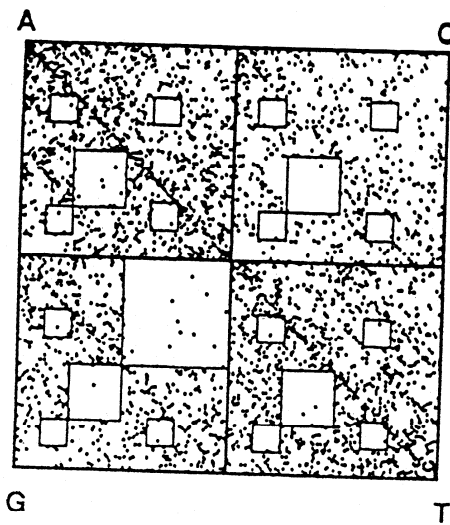


Figure 2.27 *Amylase DNA IFS square with empty regions marked.*

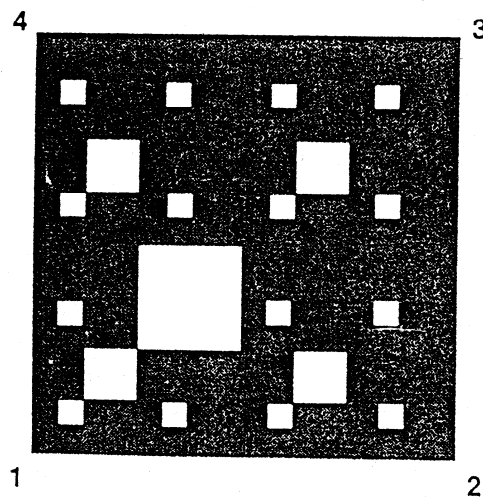


Figure 2.26 *Some holes in an otherwise filled-in square made by the random IFS algorithm plus the condition that rule 1 cannot follow rule 3.*

A NEW FAST TECHNIQUE FOR FINGERPRINT IDENTIFICATION WITH FRACTAL AND CHAOS GAME THEORY

MAHDI JAMPOUR,* MAHDI YAGHOobi
and MARYAM ASHOURZADEH

*Islamic Azad University, Mashhad Branch
Mashhad, Iran*

**Jampour@IEEE.org*

ADEL SOLEIMANI

*Islamic Azad University, Zaranb Branch
Zaranb, Iran*

Received September 12, 2009

Accepted October 25, 2009

Abstract

Fingerprints are one of the simplest and most reliable human biometric features for identification. Geometry of the fingerprint is fractal and we can classify a fingerprint database with fractal dimension, but one can't identify a fingerprint with fractal dimension uniquely. In this paper we present a new approach for identifying fingerprint uniquely; for this purpose a new fractal is initially made from a fingerprint by using Fractal theory and Chaos Game theory. While making the new fractal, five parameters that can be used in identification process can be achieved. Finally a fractal is made for each fingerprint, and then by analyzing the new fractal and parameters obtained by Chaos Game, fingerprint identification can be performed. We called this method Fingerprint Fractal Identification System (FFIS). The presented method

*Mailing address for delivery of offprints: Dr. Mahdi Jampour, Artificial Intelligence Department at Islamic Azad University of Mashhad – Mashhad-Iran. Tel: (+98) 0915-519-4189.

besides having features of fractals such as stability against turning, magnifying, deleting a part of image, etc. also has a desirable speed.

Keywords: Biometric; Fingerprint Identification; Chaos Game Theory; Fractal Dimension.

1. INTRODUCTION

These days, identification is known as an issue which is so interrelated with human biometric features that signature, face, voice, iris, fingerprint, etc. in human are used for this purpose.¹ Undoubtedly, one of the simplest and most reliable identification methods based on human biometric features is the fingerprint, which has been in use for more than a hundred years in human identification, due to its stability and unity. Identification based on fingerprints is considered as one of popular methods in identification of individuals and the simplicity of the mechanism is the cause of this popularity. Sir Francis Galton and Sir Edward Henry were the first people who worked on identification based on fingerprint.^{2,3} Galton focused his studies on fingerprint features and the results of his study led to definition and identification of some features in fingerprint and he called them *Minutiae*. Some of these features are shown in Fig. 1. Unlike him, Henry studied the general structure of fingerprint and the results of his studies led to classification of fingerprints into five categories; Fig. 2 shows this classification for fingerprints. Studies of these two were so much deep and clear that even after a hundred years they are used in researches. Issue of mechanical and automatic identification of fingerprint after extensive studies was authorized

by FBI in 1969 and after that this task was given to National Institute of Standards and Technology (NIST). Some other works have been carried out on this subject, for instance we can point to what Maltoni has done for this purpose. He and his colleagues, relying on techniques based on Minutiae which Galton had introduced, worked on basic features of fingerprint and did the identification by the aid of these features.⁴ In another work which was presented by Polikarpova, he analyzed fingerprint with fractal outlook. In this report fractal method is used for identification.⁵ Also in an article which Karki presented with the assistance of his colleagues in 2007, like Maltoni, by analyzing Minutiae and improvement of popular methods he worked on identification based on fingerprint.⁶

2. FINGERPRINT

The ins and outs on tip of fingers are called fingerprints. Based on studies of Galton, there are some features in each fingerprint which are different in various samples of fingerprints. These features are called Minutiae and on average there are about 50 to 80 features in each fingerprint.⁷⁻⁹ Core, delta, bifurcation, ridge, crossover, and island are some of these features.

2.1. Fingerprint Identification Methods

Fingerprint identification methods are often divided into two main groups¹⁰⁻¹²:

- (1) Minutiae Based Algorithm (MBA)
- (2) Pattern Based Algorithm (PBA)

In the first type a fingerprint becomes ready for processing in a pre-processing stage and then the features of that fingerprint is compared to the features of other fingerprints. However, in a pattern based method, the pattern of fingerprint sample is compared to other samples, level of conformity is calculated and on the basis of that a decision is made.




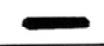


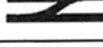
	Termination
	Bifurcation
	Lake
	Independent ridge
	Point or island
	Spur
	Crossover

Fig. 1 The most common *minutiae* types.

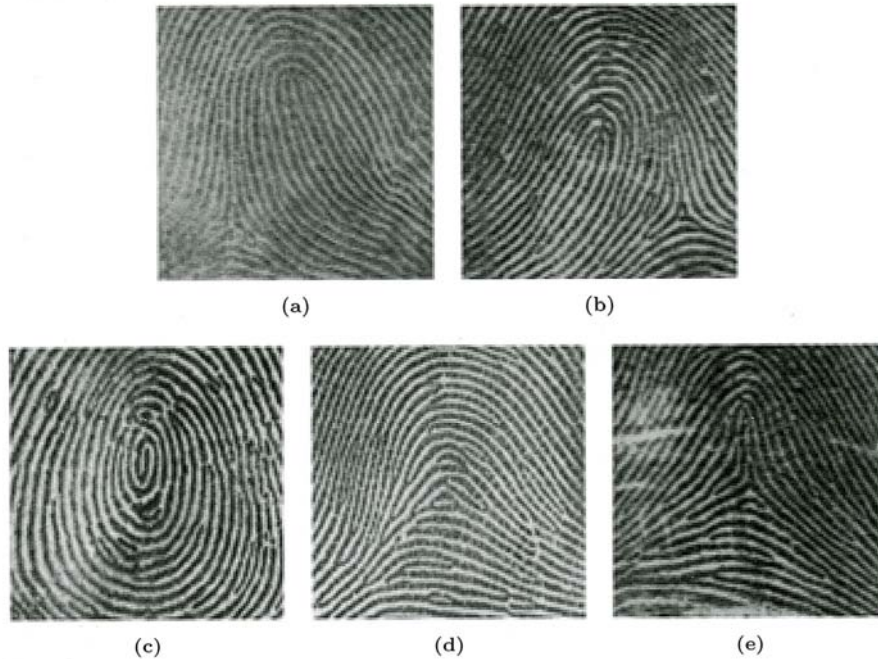


Fig. 2 Henry fingerprint classification: (a) Right loop; (b) Left loop; (c) Whorl; (d) Arch; and (e) Tented Arch.

3. FRACTAL DIMENSION

The term *fractal* was introduced by Mandelbrot for the first time in 1975^{13,14} and refers to geometry of objects which have the following features:

- (1) Self-similarity;
- (2) iterative formation; and
- (3) fractional dimension.

It means that components of a fractal object are similar to whole of that object and are produced with a repetitive procedure and more importantly, if we calculate dimension of these objects, unlike objects like a line which has just one dimension or plate for which dimension is two, the dimension of fractal objects is a decimal number. In Fig. 3 a sample fractal is shown; while Fig. 4 shows another fractal which is known as Sierpinski Triangle and it has a dimension of 1.58.

The fractal dimension is a statistical quantity that gives an indication of how completely a fractal appears to fill space, as one zooms down to finer and finer scales. As a mathematical definition it should be said that the base of most definitions of dimension is the idea of measurement in the scale of δ . For each δ , by ignoring irregularities smaller than δ , we measure a collection and we see how these collections behave when $\delta \rightarrow 0$. For instance, if F

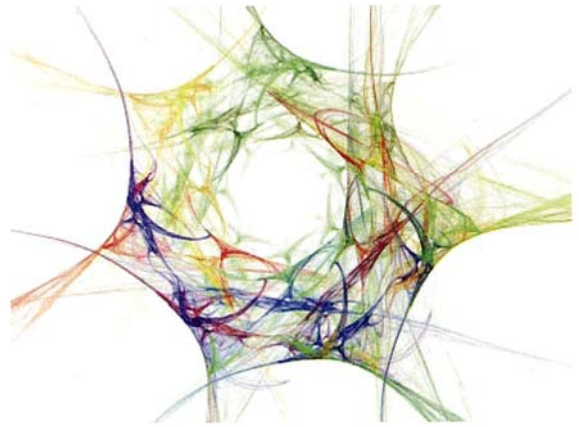


Fig. 3 Farid's fractal. (From Dr. John Daab, <http://www.fineartregistry.com/articles/art-technology/fine-art-authenticator-technology.php>.)

is a surface curve, then our measurement $M(\delta(F))$ can be the number of necessary steps for measurement or covering of F by making use of distance or length of δ .

3.1. Fractal Dimension Calculation Methods

In 1977, for the first time Mandelbrot gave a definition of fractal dimension.¹⁵ Fractals explain some

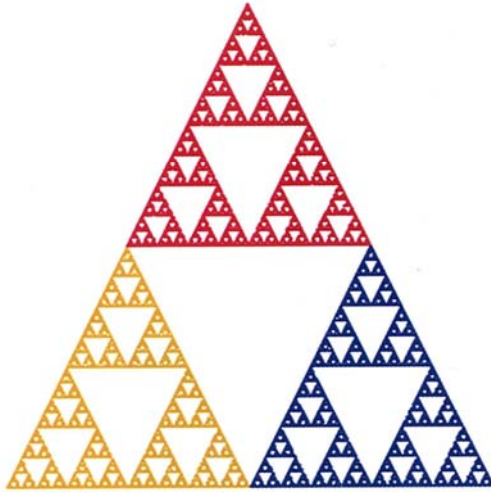


Fig. 4 Triangle, that its dimension is 1.58.

of irregular geometric features of shapes and solids which seem similar in all scales. Many of the objects around us have such complicated features that measurement of length, area, or volume with common methods are impossible. However, there is a method for measuring their geometric properties so that while measuring with higher accuracy by estimating increase of length (area, volume) this method can be obtained. The main thesis of this method is that two basic quantities — length (area, volume) — on the one hand and level of accuracy in measurement on the other hand do not change by their own will; rather they change in a way which provides the possibility of measurement of fractal dimension. This outlook is in fact the same hidden basic idea in calculation of fractal dimension.

The followings are some of the most important methods of fractal dimension calculation¹⁶:

- (1) box-counting dimension;
- (2) Hausdorff dimension;
- (3) packing dimension;
- (4) Renyi dimension; and
- (5) correlation dimension.

For example, in the Box-Counting method the proposed fractal is divided into similar boxes and then logarithm of boxes, which includes the chosen collection, is calculated in relation with logarithm of reversed ratio of size of box. This should be repeated again for other sizes of boxes and after defining the ratio shown in relation (1) in a two-dimensional graph some points would be obtained

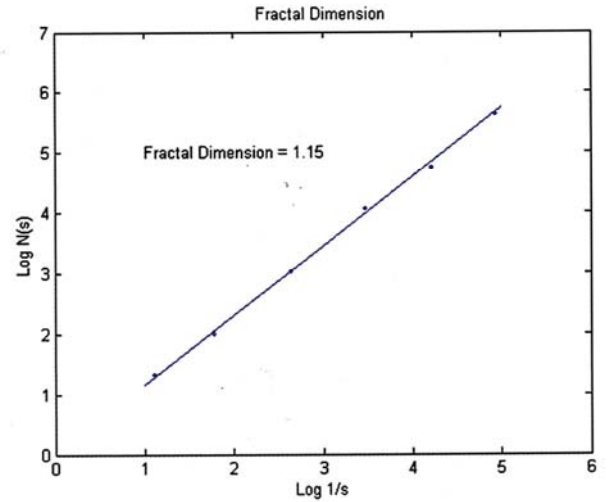


Fig. 5 Calculate fractal dimension with box-counting method.

and the slope of the line which passes these points is considered as the dimension of the proposed object. Figure 5 shows the procedure of fractal dimension calculation with Box-Counting method.

$$D = \frac{\log(N_s)}{\log(1/s)}. \quad (1)$$

3.2. Fingerprint Identification with Fractal Dimension

Fractal dimension is a statistical quantity and a part of fractal properties, and can be considered as a suitable parameter for comparing fractals so that analyzing the calculated dimension for several fingerprint samples shows their difference. However, most of the time calculating fractal dimension for more than four decimal digits is not possible; therefore it can identify at most 10,000 fingerprints and it is not sufficient for identifying fingerprints. Consequently, this fractal dimension cannot be used for fingerprint identification, but after some experiments we concluded that we can use fractal dimension for fingerprint classification, based on Henry's classification.

3.3. Chaos Game Theory

Chaos Game theory was presented by Barnsley in 1988.^{16,17} This theory on the strength of Shannon Theorem is presented in a way that by using Random Walk mechanism and by the aid of a polygonal a fractal can be produced. This theory has

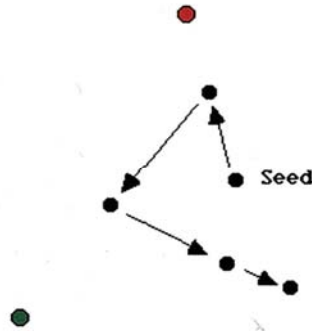


Fig. 6 Chaos Game mechanism on triangle that generate Sierpinski triangle.

two important points: first, by performing Chaos Game mechanism on a fractal a new fractal can be produced. Second and more important, while performing Chaos Game mechanism for producing the new fractal, besides properties of fractal some parameters can be achieve which would be useful in identification process. If we perform Chaos Game mechanism on a triangle, the procedure will be as the following: first, an accidental point is chosen. This point is the start point and it is not important in what situation it is. Then, in the second step an accidental number in the scope of [1, 2 or 3] is chosen. If 1 is chosen it means summit A, if 2 is chosen it means summit B, and eventually if 3 is chosen it means summit C in triangle. Then, from the present point we step forward half way toward chosen summit and draw a new point. Again, we make an accidental choice and repeat the same process for several times (for example 50,000 times). This way a shape which is the Sierpinski Triangle is drawn. In Fig. 6 four steps of Chaos Game mechanism are shown.

4. MAKING NEW FRACTAL BASED ON FINGERPRINT

A fingerprint is a fractal and from fractal outlook it has fractal dimension parameter which is not sufficient for identification. As mentioned in Sec. 3.2, by the aid of Chaos Game a new fractal can be made and while making the new fractal more parameters can be obtained. As a result, based on a fingerprint and a pattern which will be pointed at afterwards the new fractal is made. The mechanism is such that a pixel of fingerprint is selected by chance. A point has 2 states: first, the pixel can be an in or zero or it might be an out or 1. Both of these states

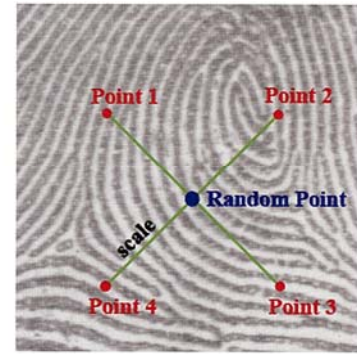


Fig. 7 Position of four assistant point's base on Random Point.

cannot be sufficient for identification, so an accidental point is chosen and based on a new parameter, which is called Scale, we find four points around the aforementioned accidental point. If accidental point is $A[i, j]$, four points will be:

$$\begin{aligned} \text{Point1} &= A[i - \text{Scale}, j - \text{Scale}]; \\ \text{Point2} &= A[i + \text{Scale}, j - \text{Scale}]; \\ \text{Point3} &= A[i + \text{Scale}, j + \text{Scale}]; \\ \text{Point4} &= A[i - \text{Scale}, j + \text{Scale}]. \end{aligned}$$

These four points are shown in Fig. 7. Having these four points, 16 states are made which we divide into five distinct groups. First group is the state where pixels of all these four points are white, second group is the state where just one pixel from the mentioned points is black and all others are white. Third group is the state where the number of points with black pixels is two, fourth group is the state where the number of points with black pixels is three, and finally fifth group is a group where all four points have black pixels. Considering binary structure, these four points and creation of sixteen possible states, all of them and their assortment based on the mentioned classification are shown in Table 1. Sixteen created states in Table 1 make five groups and for making a new fractal in Chaos Game process we use a square which is shown with five tips in Fig. 8. These five tips are named with alphabets to make the new fractal image which is obtained from the fingerprint. The result of fractal which is made by the above procedure for several samples of fingerprints is shown in Fig. 9.

5. PARAMETERS EXTRACTION

As mentioned before, while making new fractal Chaos Game mechanism, new parameters are

Table 1 Category of Different State of Points.

Points 1-4	Category	Points 1-4	Category
0 0 0 0	1	1 0 0 0	2
0 0 0 1	2	1 0 0 1	3
0 0 1 0	2	1 0 1 0	3
0 0 1 1	3	1 0 1 1	4
0 1 0 0	2	1 1 0 0	3
0 1 0 1	3	1 1 0 1	4
0 1 1 0	3	1 1 1 0	4
0 1 1 1	4	1 1 1 1	5

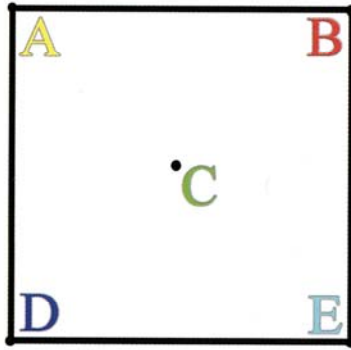


Fig. 8 Five points that are mapped on five categories in Table 1.

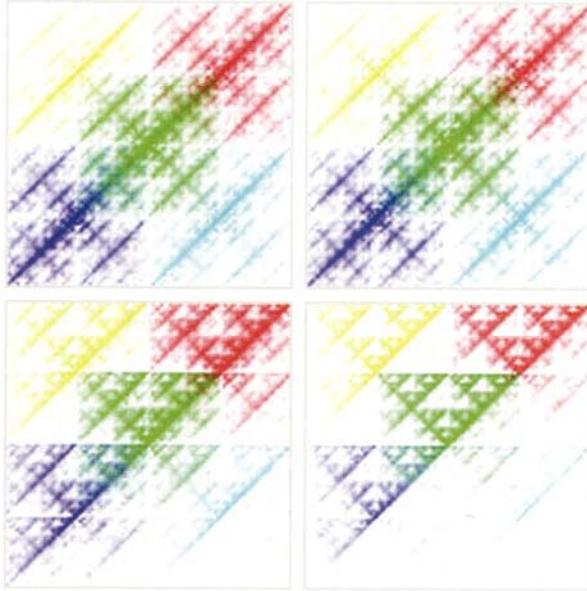


Fig. 9 Four fractals that generated from four fingerprints.

obtained which can be useful in identification. In part four it was cited that regarding four defined points for pixels of those points, five states can be created which are classified into category1 to

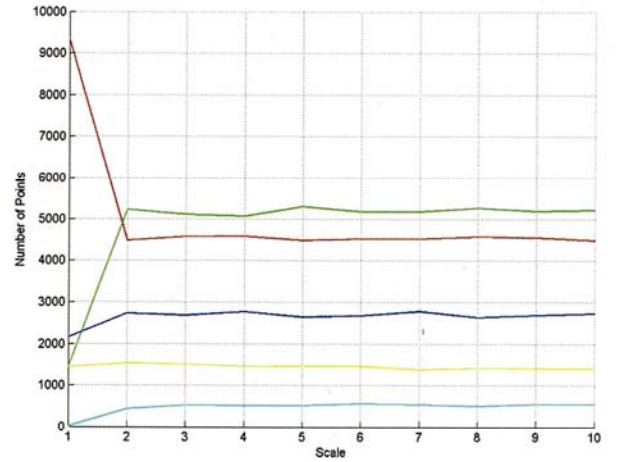


Fig. 10 Spectrums of a fingerprint.

category5. Then, we repeat Chaos Game mechanism 100,000 times and in each repetition by identifying four pixels of the points one of possible states is chosen and one unit is added to the counter of that category. This way, at the end of Chaos Game mechanism total of all five categories is equal to the number of repetitions, *i.e.* 100,000. By dividing each of categories by 100,000 they are standardized and we state them in the zero to one span. Therefore, for each fixed quantity for Scale parameter, which is the distance of points to the accidental point, five parameters are calculated. As five parameters with accuracy of (0.02) are not enough for identification, the above mentioned procedure is calculated for quantities of 10 and 15 for Scale.

As a result, we will have ten parameters and considering the accuracy of 0.02 in the span of zero to one we will have 50 varieties. By having ten parameters we will reach $50^{10} = 9.76 \times 10^{16}$ varieties for fingerprints, which guarantees unity of fingerprints. On the other hand, if we calculate Scale with different quantities for a fingerprint, we will have five independent spectrums and with the accuracy of 0.02 these spectrums are able to identify fingerprint based on the given mechanism. Figure 10 illustrates spectrums of parameters which are obtained from a sample fingerprint.

6. IMPLEMENTATION

The presented technique in this report (FFIS) has been carried out by MATI/AB and has been experimented on 600 samples of fingerprints,¹⁸ of which there are four samples of each. A sample of images used is shown in Fig. 11. Results obtained show

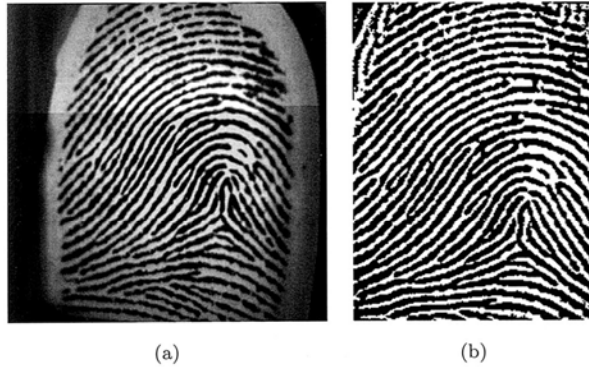


Fig. 11 (I) Before preprocessing, and (II) after preprocessing.

Table 2 Result of Search and Feature Extraction.

Fingerprint Name	FEST (ms)*	ST (ms)**
Fig1001B1	1839	32
Fig1152B1	1906	32
Fig1263B1	1870	31
Fig1484B1	1898	34
Fig1545B1	1901	31
Fig1001B2	1885	32
Fig1001B5	1863	33

*FEST: Feature Extraction and Save Time (millisecond).

**ST: Search Time in 600 Samples (millisecond).

100% success for this technique. In another experiment 50 samples of fingerprints for which 20% of image was accidentally deleted were analyzed with the remaining parts, and again 100% success was obtained and this shows stability of the presented method encountering deletion of some parts of image. Table 2 illustrates data related to time of searching in a database, which includes 600 samples, and also information related to time of deciphering and saving features of fingerprint in a database for some fingerprint samples. It must be noted that the experimenting system had a CPU Intel Celeron 2.60, 512 MB RAM and Windows XP as its operating system.

7. CONCLUSION

Identification process by fingerprint based on popular methods such as Minutiae Based Algorithm and Pattern Based Algorithm is a time consuming process; thus, it encourages researchers to study new methods with more efficiency. As the fingerprint is a fractal, properties of fractals can be used in analysis of fingerprints. One of these properties is fractal

dimension calculation, which because of low level of accuracy cannot be efficient in identification, but it can be used in classification. From other properties of fractals deciphering features through Chaos Game mechanism can be relied on. In this mechanism, as many as required features of fingerprint are achieved. We have extracted five features with various scales and with accuracies of 0.02. This led to a great variety and in this way we can guarantee keeping the unity of fingerprint in presented technique. Using the presented process in this study has led to expansion of efficiency of automatic systems in identifying human by fingerprints and the speed which is presented in this system is our basic proposed expansion.

8. FURTHER RESEARCH

The outlook presented in this study has provided a new viewpoint for analyzing fractals and by using Chaos Game mechanism new features have been extracting for each fractal. Therefore, it can be useful in cases such as classification of histopathology slides in medicine, generation of new music, generation of various art forms, signal and image compression, fractal antennas, technical analysis of price series, etc.^{19,20}

REFERENCES

1. A. K. Jain, P. J. Flynn and A. A. Ross, *Handbook of Biometrics* (Springer, New York, 2008).
2. F. Galton, *Finger Prints* (McMillan, London, 1892).
3. E. Henry, *Classification and Uses of Finger Prints* (Routledge, London, 1900).
4. D. Maltoni, D. Maio, A. Jain and P. Prabhakar, *Handbook of Fingerprint Recognition* (Springer, New York, 2003).
5. N. Polikarpova, On the fractal features in fingerprint analysis, in *The 13th International Conference on Pattern Recognition (ICPR'96)*, Vol. 3 (Vienna, Austria, 1996) pp. 591.
6. M. V. Karki and S. Sethu, A novel fingerprint recognition system with direction angles difference, in *The International Conference on Computational Intelligence and Multimedia Applications (ICCIMA 2007)* (Sivakasi, Tamilnadu, India) pp. 501.
7. M. Jampour, Fingerprint recognition with fractal theory, MSc. Thesis (Islam. Azad Univ. Mashhad. Iran, 2009).
8. M. Jampour, H. Shojaei, M. Ashourzadeha and M. Yaghobi, Compressing of fingerprint images by means of fractals feature, in *The Second International Conference on Machine Vision (ICMV'09)* (Dubai, 2009) pp. 18–22.

9. S. Chikkerur, S. Pankanti, A. Jea, N. Ratha and R. Bolle, Fingerprint representation using localized texture features, in *The 18th International Conference Pattern Recognition (ICPR'06)*, Vol. 4 (Hong Kong, 2006) pp. 521.
10. H. Guo, A Hidden Markov Model fingerprint matching approach, in *Proceedings of the 2005 International Conference on Machine Learning and Cybernetics*, Vol. 8 (Guangzhou, China, 2005) pp. 5055–5059.
11. J. Zhou and G. Jinwei, A model-based method for the computation of fingerprints' orientation field, *IEEE Trans. Image Process.* **13**(6) (2004) 821.
12. L. Nanni and A. Lumini, Local binary patterns for a hybrid fingerprint matcher, *J. Pattern Recog.* **41**(11) (2008) 3461.
13. B. Mandelbrot, *Fractals: Form, Chance, and Dimension* (W. H. Freeman and Co, San Francisco, 1977).
14. B. Mandelbrot, A multifractal walk down Wall Street, *Sci. Am.* **280**(2) (1999) 70.
15. J. Kigami, *Analysis on Fractals* (Cambridge University Press, Cambridge, 2001).
16. M. F. Barnsley, *Fractals Everywhere* (Academic Press, New York, 1988).
17. M. F. Barnsley, *SuperFractals* (Cambridge University Press, New York, 2006).
18. C. Brislawn, The FBI Fingerprint Image Compression Standard, <http://www.c3.lanl.gov/~brislawn/FBI/FBI.html>.
19. M. Jampour, M. Yaghobi and M. Ashourzadeh, Fractal images compressing by estimating the closest neighborhood with assistance of schema theory, *J. Comput. Sci.* **6**(5) (2010) 591–596.
20. M. Jampour et al., Compressing images using fractal characteristic by estimating the nearest neighbor, in *Proceedings of the 2009 Sixth International Conference on Information Technology: New Generations* (IEEE Computer Society, Washington, DC, USA) pp. 1319–1322.

Bacterium-Phage Interactions

Multi-Species Model of Bacterium-Phage Interaction

$$\frac{dI_{i3}}{dt} = \frac{3}{\tau_i} (I_{i2} - I_{i3}) - \rho I_{i3}, \quad (6.17)$$

$$\frac{dP_j}{dt} = \phi_j - P_j \left[\sum_{i=1}^3 \alpha_{ij} B_i + \rho + \sum_{i,k=1}^3 \alpha_{ij} I_{ik} \right] + 3\beta_j I_{j3} / \tau_j, \quad (6.18)$$

$$\frac{dS}{dt} = \rho (\sigma - S) - \sum_{i=1}^3 \frac{v_i \gamma_i S B_i}{\kappa_i + S}. \quad (6.19)$$

Here, ϕ_j is a small external supply of phages, and β is the burst size. While all other variables in the model are treated as deterministically determined mean values, ϕ_j is a Poisson distributed stochastic variable with an average value of $\phi = 0.1 / \text{ml} \cdot \text{min}$ for all phage variants. Clearly, ϕ is only significant as a source of infection.

Altogether, this leads to the following set of differential equations

$$\frac{dB_i}{dt} = \frac{v_i S B_i}{\kappa_i + S} - B_i \left(\rho + \sum_{j=1}^3 \alpha_{ij} \omega_{ij} P_j \right), \quad (6.14)$$

$$\frac{dI_{i1}}{dt} = B_i \sum_{j=1}^3 \alpha_{ij} \omega_{ij} P_j - \rho I_{i1} - 3I_{i1} / \tau_i, \quad (6.15)$$

$$\frac{dI_{i2}}{dt} = \frac{3}{\tau_i} (I_{i1} - I_{i2}) - \rho I_{i2}, \quad (6.16)$$

Multi-Species Model of Bacterium-Phage Interaction

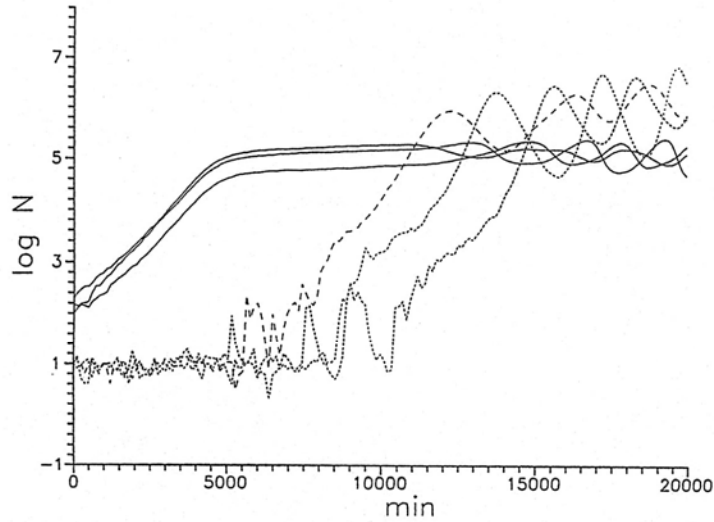


FIGURE 6.8 Results of a simulation in which the rate of dilution is gradually reduced from 0.011/min to 0.007/min over a period of 20,000 min. The vertical axis shows the concentrations of bacteria and viruses on a logarithmic scale. As the viral populations reach macroscopically significant levels, the system becomes unstable and starts to produce self-sustained oscillations. Full curves for the three bacterial variants; dotted curves for the corresponding viruses.

Multi-Species Model of Bacterium-Phage Interaction

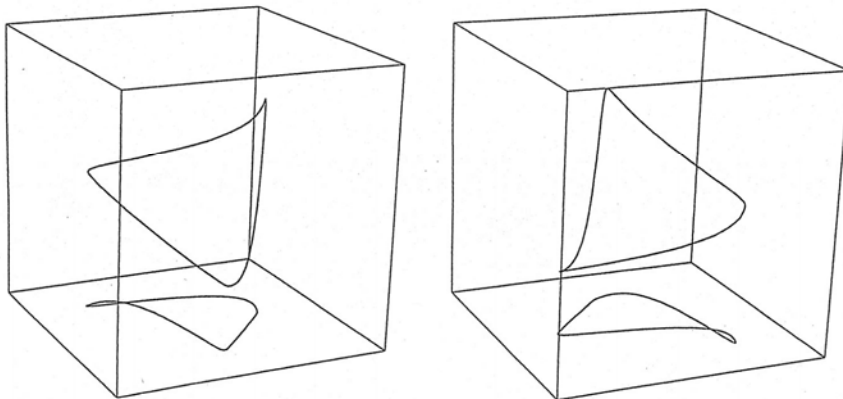


FIGURE 6.9 Three-dimensional phase plots of the symmetric periodic solutions which exist for a dilution rate of $\rho = 0.0065/\text{min}$. As axes we have used the three bacterial populations on a logarithmic scale. The existence of two symmetric attractors is characteristic of systems where rotation in one or the other direction are equally possible.

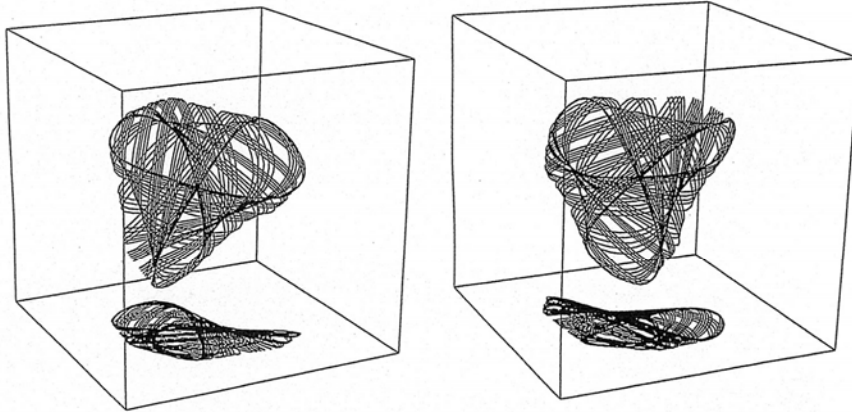


FIGURE 6.10 Three-dimensional phase plots of the two symmetric quasi-periodic solutions which exist for $\rho = 0.0055/\text{min}$. Interestingly enough, the periodic solutions shown in Fig. 6.10 still exist as stable attractors.

The Chaotic Hierarchy

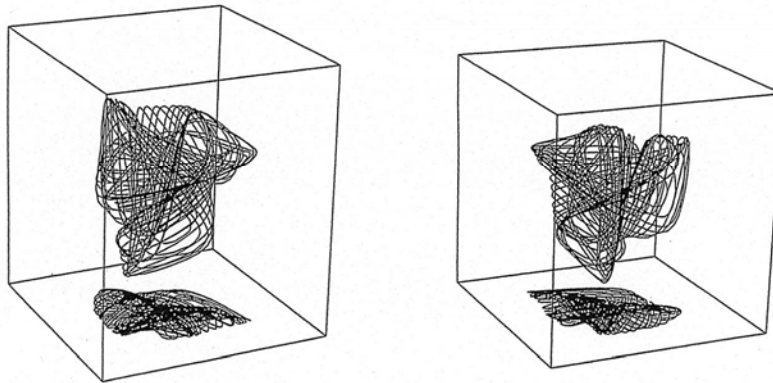


FIGURE 6.11 Three-dimensional phase plots of the two symmetric chaotic solutions which exist for $\rho = 0.0045/\text{min}$. The periodic solutions of Fig. 6.10 still exist and can be reached from particular sets of initial conditions. In the next section we shall describe how the chaotic solutions develop out of the quasiperiodic solutions in Fig. 6.10.

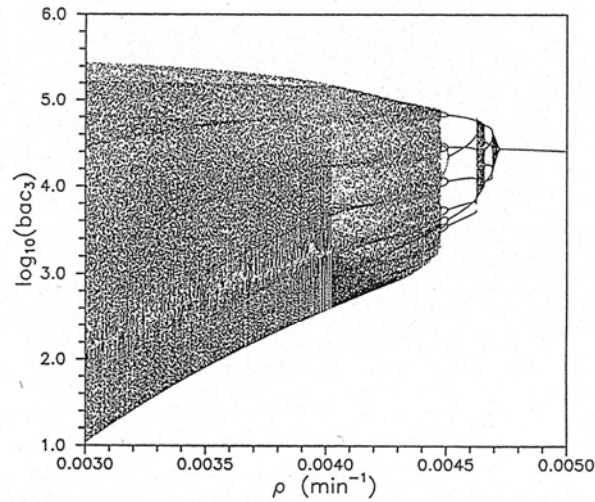


FIGURE 6.12 Bifurcation diagram for a system with two bacterial populations. With initial conditions $(S)_0 = 0.0$, $(B_1)_0 = 25000/\text{ml}$ and $(B_2)_0 = 25118/\text{ml}$, the simulation has been started at $\rho = 0.0050/\text{min}$ and the stationary solution followed adiabatically with a step size of $\Delta\rho = 2.0 \cdot 10^{-6}/\text{min}$. For each value of ρ a transient of 105 min was omitted, and subsequent steady state intersection points with the Poincaré plane $B_1 = B_2$ were plotted. Vanishing initial populations of phages and infected bacteria were assumed.

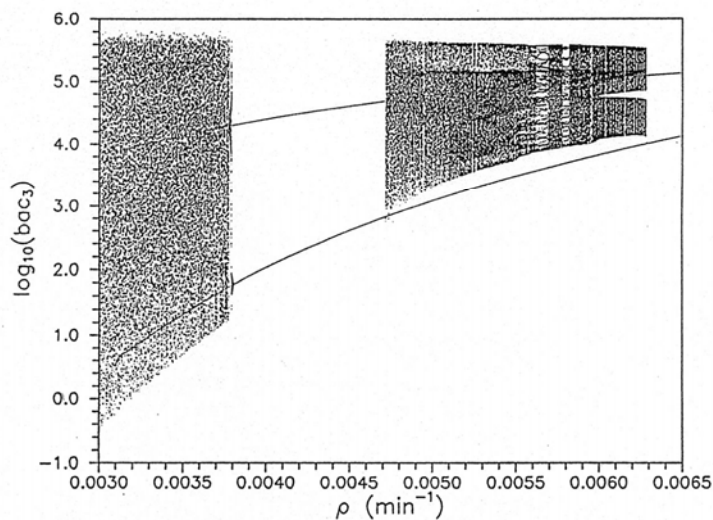


FIGURE 6.16 Bifurcation diagram for the three-population model. Several branches obtained with different initial conditions have been plotted on top of each other. For $\rho < 0.0030/\text{min}$, only hyperchaos with two positive Lyapunov exponents is found.

Tango waves in a bidomain model of fertilization calcium waves

Yue-Xian Li*

*Departments of Mathematics and Zoology, University of British Columbia, No. 121-1984 Mathematics Road,
Vancouver, BC, Canada V6T 1Z2*

Received 9 December 2002; received in revised form 31 May 2003; accepted 30 June 2003
Communicated by J.P. Keener

This work is dedicated to Joel Keizer whose support, encouragement, and valuable advice had been indispensable for the discovery reported in this work

Abstract

Fertilization of an egg cell is marked by one or several Ca^{2+} waves that travel across the intra-cellular space, called fertilization Ca^{2+} waves. Patterns of Ca^{2+} waves observed in mature or immature oocytes include traveling fronts and pulses as well as concentric and spiral waves. These patterns have been studied in other excitable media in physical, chemical, and biological systems. Here, we report the discovery of a new wave phenomenon in the numerical study of a bidomain model of fertilization Ca^{2+} waves. This wave is a front that propagates in a back-and-forth manner that resembles the movement of tango dancers, thus is called a tango wave. When the medium is excitable, a forward-moving tango wave can generate traveling pulses that propagate down the space without reversal. The study shows that the occurrence of tango waves is related to spatial inhomogeneity in the local dynamics. This is tested and confirmed by simulating similar waves in a medium with stationary spatial inhomogeneity. Similar waves are also obtained in a FitzHugh–Nagumo system with a linear spatial ramp. In both the bidomain model of Ca^{2+} waves and the FitzHugh–Nagumo system, the front is stable when the slope of a linear ramp is large. As the slope decreases beyond a critical value, front oscillations occur. The study shows that tango waves facilitate the dispersion of localized Ca^{2+} . Key features of the bidomain model underlying the occurrence of tango waves are revealed. These features are commonly found in egg cells of a variety of species. Thus, we predict that tango waves can occur in real egg cells provided that a slowly varying inhomogeneity does occur following the sperm entry. The observation of tango wave-like waves in nemertean worm and ascidian eggs seems to support such a prediction.

© 2003 Elsevier B.V. All rights reserved.

Because Ca^{2+} levels in both domains are finite in the bidomain model, we can introduce a new variable z , called the total Ca^{2+} concentration at each space point:

$$z = c + \sigma c_e, \quad (4)$$

where the volume ratio σ plays the role of a volume converting factor. Thus, σc_e represents the Ca^{2+} concentration in the ER measured by the cytosolic volume instead of the ER volume. Replacing c_e by z in (1)–(3), we obtain

$$\frac{\partial c}{\partial t} = \left[l + p \left(\frac{ch}{c+a} \right)^3 \right] (z - sc) - \frac{vc^2}{c^2 + k^2} + D \nabla^2 c, \quad (5)$$

$$\frac{\partial z}{\partial t} = (D - D_e) \nabla^2 c + D_e \nabla^2 z, \quad (6)$$

$$\frac{\partial h}{\partial t} = g[1 - (1 + c)h], \quad (7)$$

where $l = L/\sigma$, $p = P/\sigma$, and $s = 1 + \sigma$. Note that Eq. (6) is actually a linear equation with a clear physical meaning. It says that a change in the value of z can only be caused by Ca^{2+} diffusion but not by Ca^{2+}

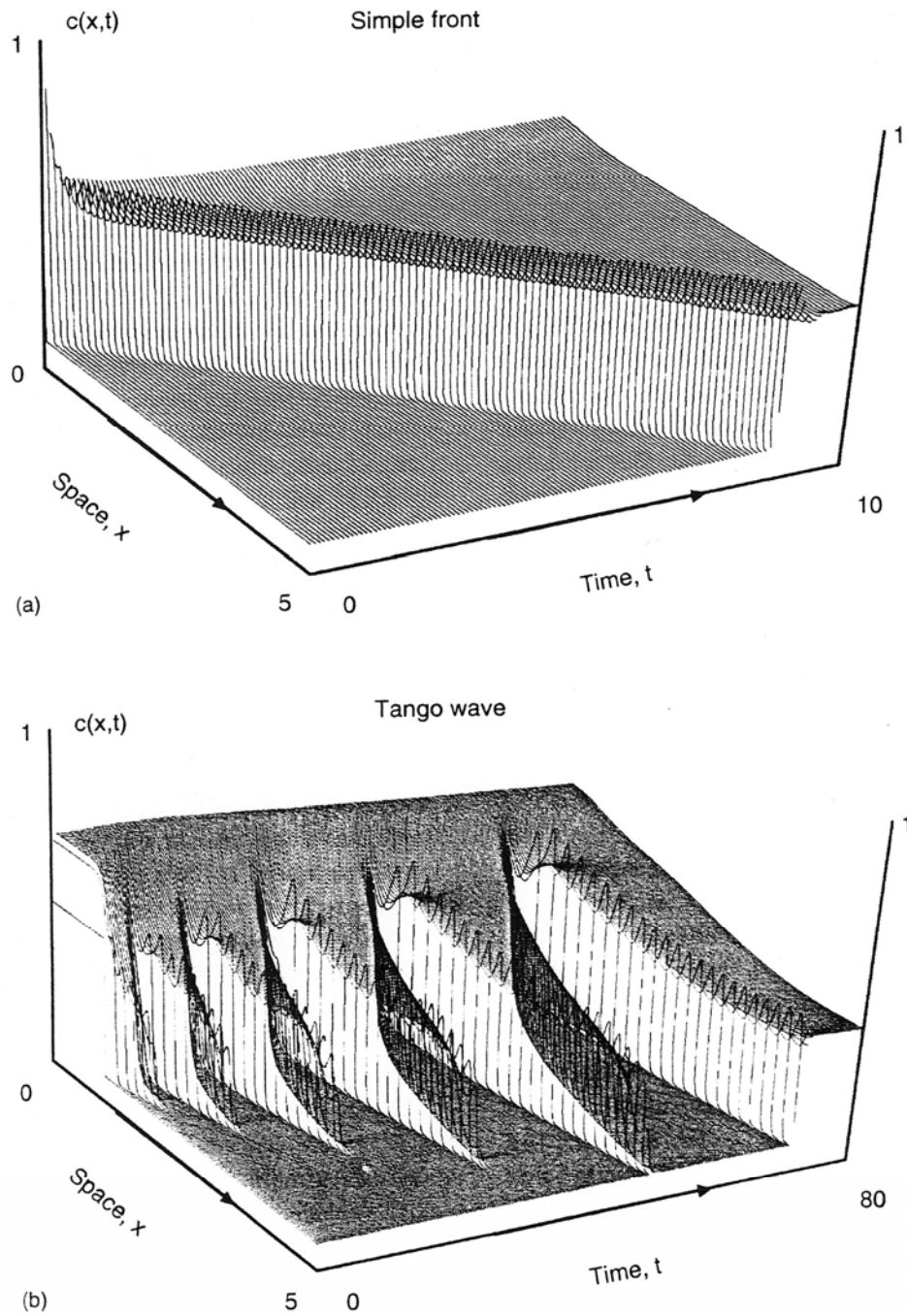


Fig. 3. (a) A simple front generated by a super-threshold stimulus in a bistable medium. (b) A tango wave generated by introducing a large amount of Ca^{2+} into a medium that is neither bistable nor excitable. Parameter values used are the same as in Fig. 2a, except that before the stimulus is applied, $z = 1.743$ in (a) and $z = 1.648$ in (b).

Period-doubling cascades and strange attractors in the triple-well ϕ^6 -Van der Pol oscillator

Jun Yu^{1,2}, Rongbo Zhang¹, Weizhen Pan¹ and L Schimansky-Geier²

¹ Department of Physics, Shaoxing University, Shaoxing 312000, People's Republic of China

² Institute of Physics, Humboldt-University at Berlin, Newton strasse 15, 12489 Berlin, Germany

Received 23 November 2007

Accepted for publication 23 June 2008

Published 31 July 2008

Online at stacks.iop.org/PhysScr/78/025003

Abstract

Duffing–Van der Pol equation with the fifth nonlinear-restoring force is investigated. The bifurcation structure and chaotic motion under the periodic perturbation are obtained by numerical simulations. Numerical simulations, including bifurcation diagrams, Lyapunov exponents, phase portraits and Poincaré maps, exhibit some new complex dynamical behaviors of the system. Different routes to chaos, such as period doubling and quasi-periodic routes, and various kinds of strange attractors are also demonstrated.

Here, we consider the extended DVP oscillator by introducing a quintic term described by the equation

$$\ddot{x} - \mu(1 - x^2)\dot{x} + \omega_0^2 x + \beta x^3 + \delta x^5 = f \cos \omega t, \quad (2)$$

where δ is a constant parameter. The potential is of ϕ^6 type, given by

$$V(x) = \frac{\omega_0^2}{2}x^2 + \frac{\beta}{4}x^4 + \frac{\delta}{6}x^6. \quad (3)$$

Depending on the set of parameters, at least three physically interesting configurations can be considered, wherein the potential is (i) single-well, (ii) double-well and (iii) triple-well. Each one of the above three cases has become a central model to describe inherently nonlinear phenomena, exhibiting a rich and baffling variety of regular and chaotic motions. Throughout this paper, our analysis is of the triple-well case.

This ϕ^6 -potential system has attracted much attention [21–23], because it is a universal nonlinear differential equation, and many nonlinear oscillators in physical, engineering and biological problems can really be described by the model or analogous ones.

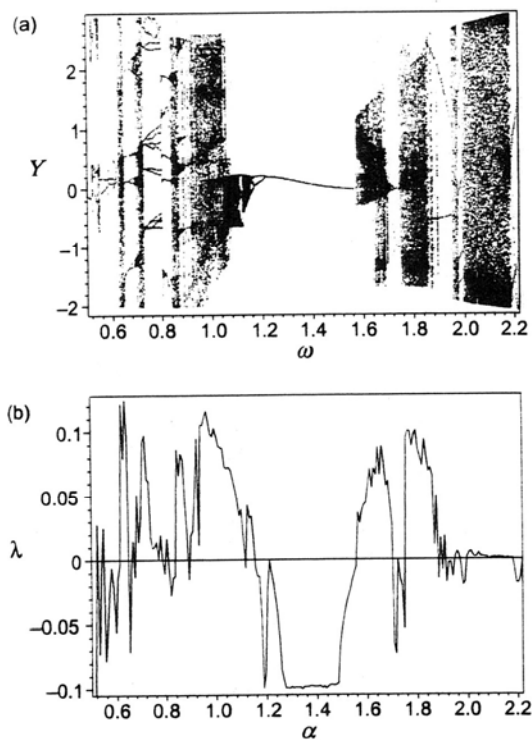


Figure 1. (a) Bifurcation diagram of (4) in the $(\alpha - Y)$ plane for $f = 1.0$, $\mu = 0.3$, $\beta = -1.8$, $\delta = 0.6$ and $\omega = 0.6$. (b) The largest Lyapunov exponents corresponding to (a).

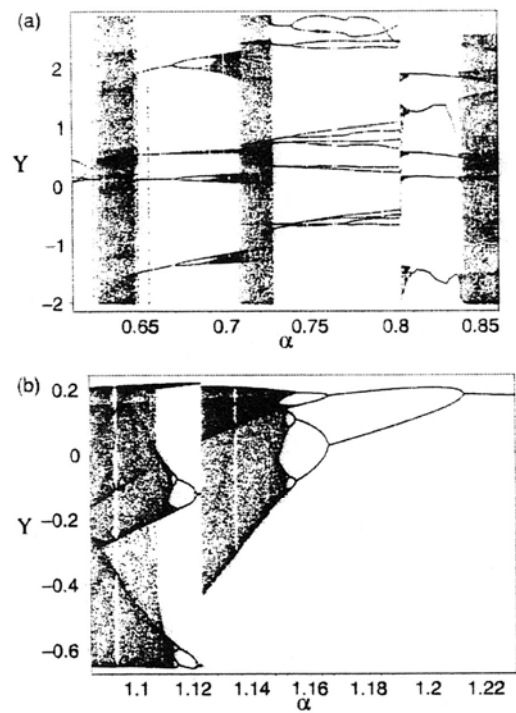


Figure 2. Local amplifications of figure 1(a): (a) $\alpha \in (0.610, 0.860)$; (b) $\alpha \in (1.085, 1.230)$.

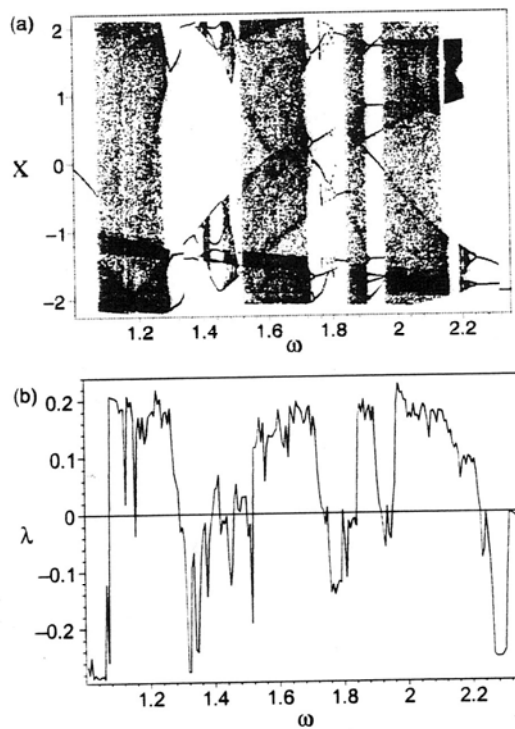


Figure 4. (a) Bifurcation diagram of (4) in the $(\omega - X)$ plane for $f = 1.00$, $\mu = 0.38$, $\alpha = 0.25$, $\beta = -0.58$ and $\delta = 0.16$. (b) The largest Lyapunov exponents corresponding to (a).

The Nonlinear Dynamics of Filaments

ALAIN GORIELY and MICHAEL TABOR

*Department of Mathematics and Program in Applied Mathematics, University of Arizona,
Building #89, Tucson, AZ 85721, U.S.A.*

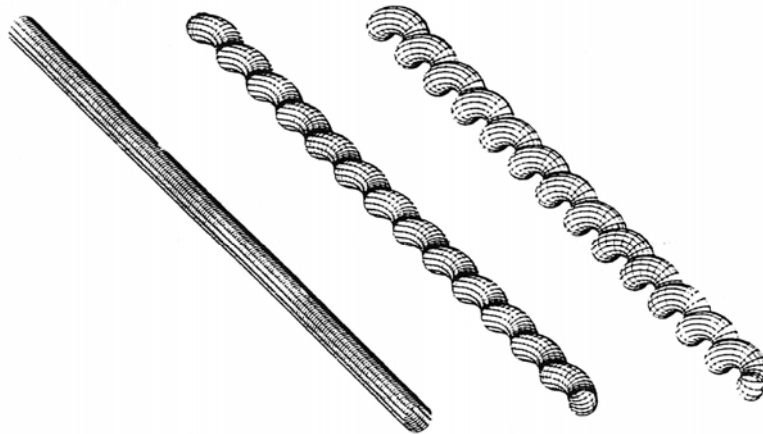


Figure 6. Perturbation of a straight rod for $n_c = 5$, $\gamma_c = 8$, $P = 3$. From left to right $A\varepsilon = 0, 0.3, 0.6$.

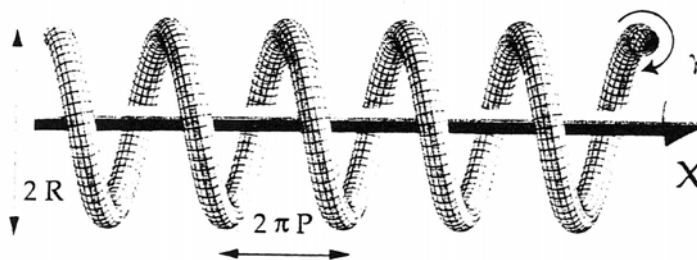


Figure 7. A helical rod characterized by an applied twist γ , a radius R , and a loop-to-loop distance $2\pi P$.

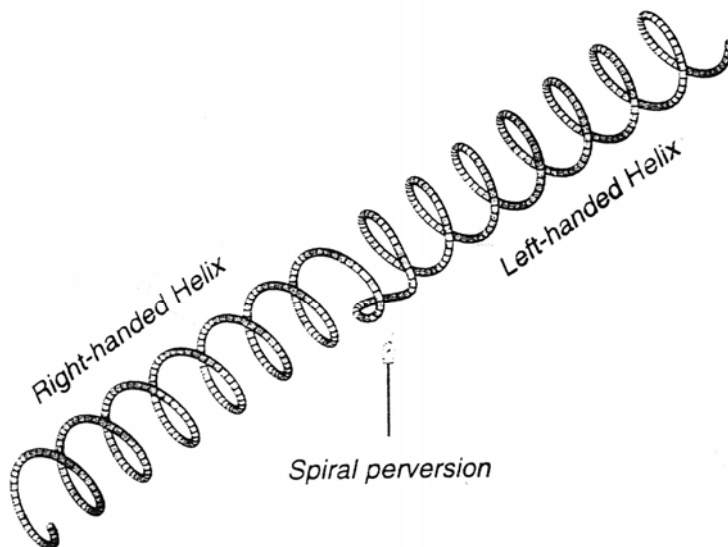


Figure 14. Sketch of a helix hand reversal.

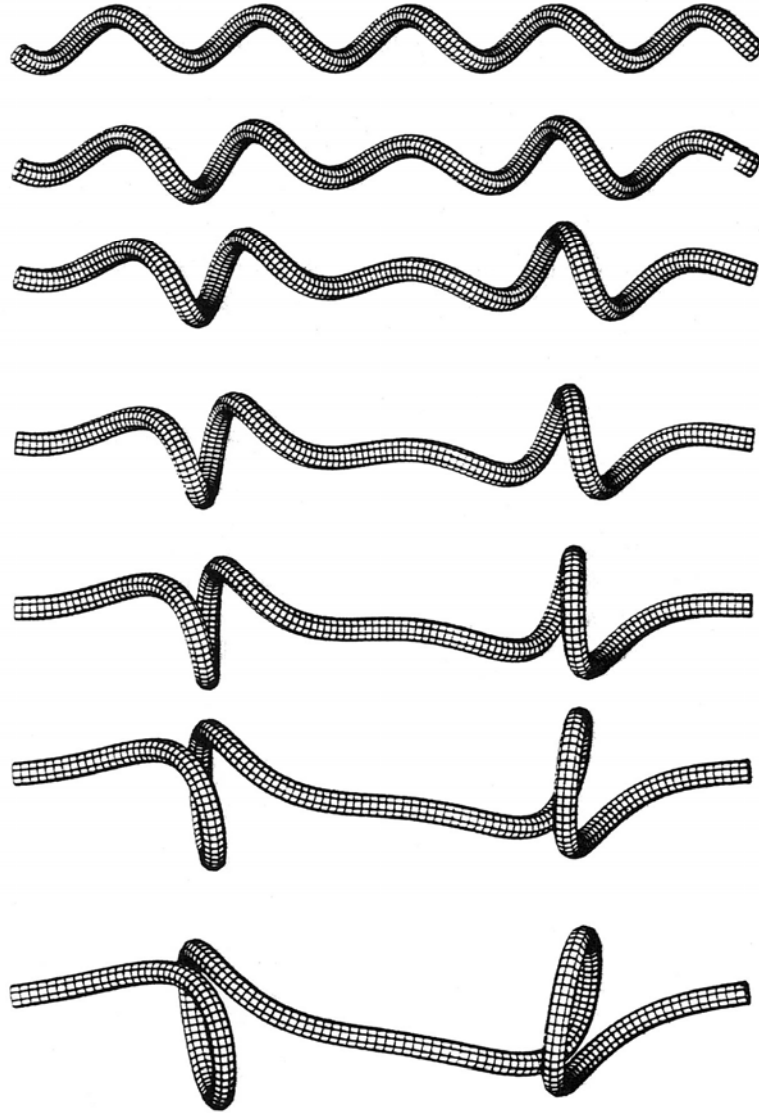


Figure 9. The time evolution of an unstable (naturally straight) helix. The linear mode $n = 2$ creates two loops ($\kappa_F = 1/8$, $\tau_F = 1/8$, $N = 5$ and $K/1000 = 0, 2, 4, 6, 8, 10, 12$). This linear mode might not represent the true evolution of the nonlinear equations and is *a priori* only valid for small values of K (see Section 5).

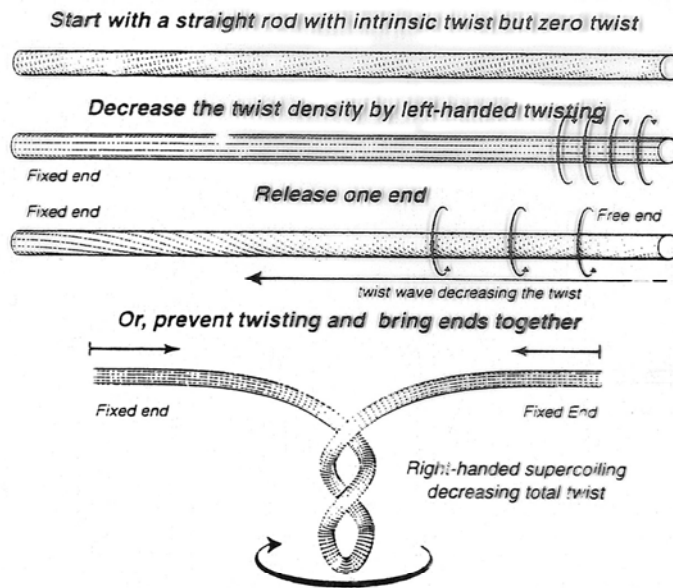


Figure 17. Twist to writhe conversion with intrinsic twist.

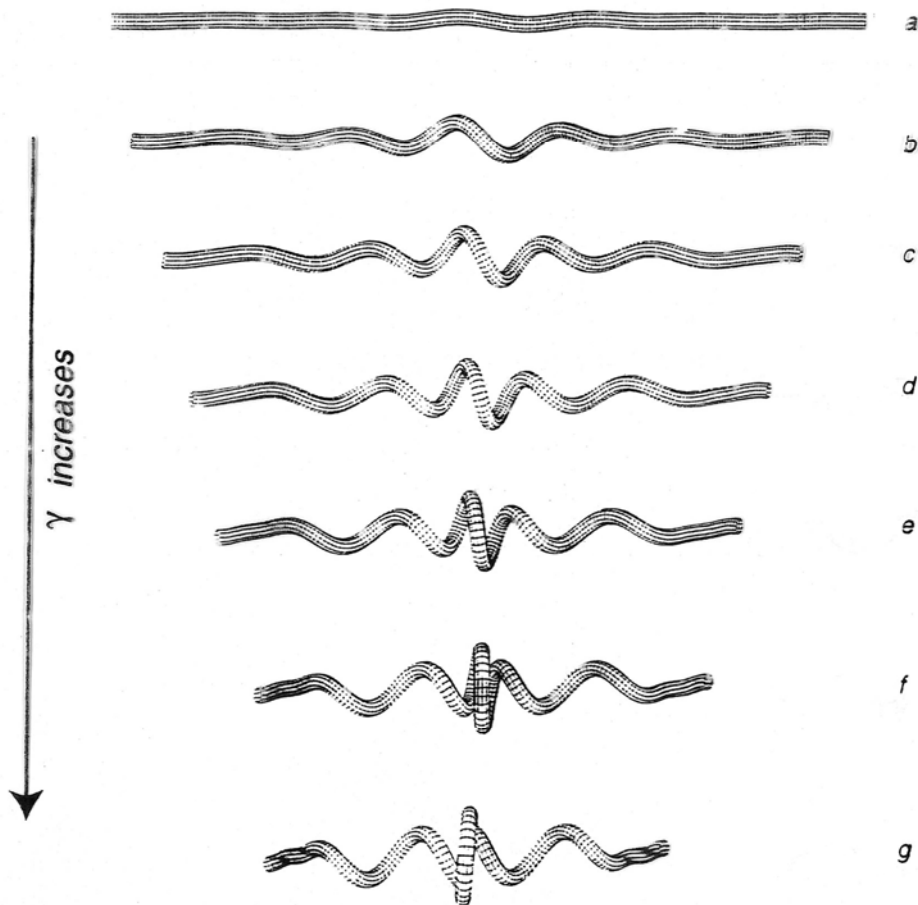


Figure 12. A sequence of helical filaments for varying values of γ_5 . (a) $\gamma_5 < \gamma_1$. (b) $\gamma_1 < \gamma_5 < \gamma_2$. (c) $\gamma_2 < \gamma_5 < \gamma_3$. (d) $\gamma_5 = \gamma_3$. (e) $\gamma_5 > \gamma_3$. The parameters are $\Gamma = 3/4$, $P = 1/10$, $N = 5$, $\gamma_1 = 0.2667$, $\gamma_2 = 0.2684$, $\gamma_3 = 0.27376$, and $\gamma_5 = \gamma_2 + \mu$ with $\mu \times 10^3 = 0.1, 1.5, 3, 4.9, 5.36, 5.4$.

Ökosüsteemide dünaamika

Producer-Consumer Dynamics

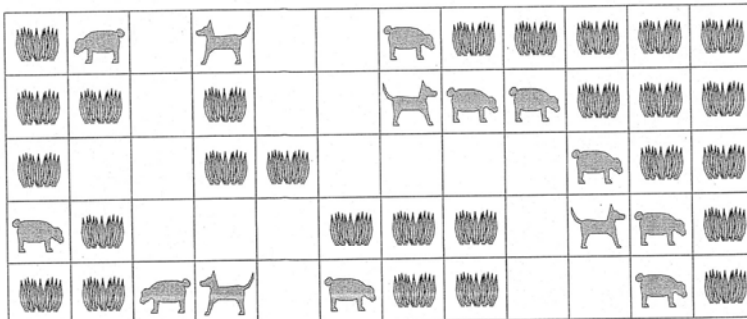


Figure 12.5 An individual-based three-species ecosystem

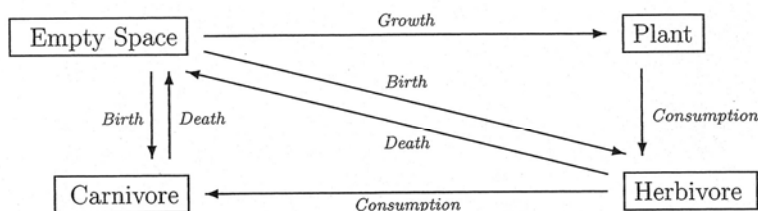


Figure 12.6 Flow of resources in the three-species individual-based ecosystem

- For every time step:
 - For every empty cell, e :
 - If e has three or more neighbors that are plants, then e will become a plant at the next time step (assuming it isn't trampled by a herbivore or carnivore).
 - For every herbivore, h (in random order):
 - Decrease energy reserves of h by a fixed amount.
 - If h has no more energy, then h dies and becomes an empty space.
 - Else, if there is a plant next to h , then h moves on top of the plant, eats it, and gains the plant's energy.
 - If h has sufficient energy reserves, then it will spawn a baby herbivore on the space that it just exited.
 - Else, h will move into a randomly selected empty space, if one exists, that is next to h 's current location.
 - For every carnivore, c (in random order):
 - Decrease energy reserves of c by a fixed amount.
 - If c has no more energy, then c dies and becomes an empty space.
 - Else, if there is a herbivore next to c , then c moves on top of the herbivore, eats it, and gains the herbivore's energy.
 - If c has sufficient energy reserves, then it will spawn a baby carnivore on the space that it just exited.
 - Else, c will move into a randomly selected empty space that is next to c 's current location. If there are no empty spaces, then c will move through plants.

Table 12.1 Update algorithm for individual-based ecological model

differential equations for an n -species predator-prey system as

$$\frac{dx_i}{dt} = x_i \sum_{j=1}^n A_{ij}(1 - x_j),$$

where x_i represents the i th species and A_{ij} represents the effect that species j has on species i and plays the same role that the parameters in the last section did. Representing the A_{ij} terms as a matrix, we can list all of the parameters as

$$\mathbf{A} = \begin{bmatrix} A_{11} & A_{12} & A_{13} \\ A_{21} & A_{22} & A_{23} \\ A_{31} & A_{32} & A_{33} \end{bmatrix} = \begin{bmatrix} 0.5 & 0.5 & 0.1 \\ -0.5 & -0.1 & 0.1 \\ \alpha & 0.1 & 0.1 \end{bmatrix}$$

The values listed in the matrix above were found by Arneodo, Couillet, and Tresser to have chaotic dynamics. Notice that the whole system is now parameterized by a single variable, α , which we can set to make the system behave in any number of ways. Setting α to 1.5 forces the system into chaotic behavior. The attractor at this value is shown in Figure 12.2. The time evolution of the three species is shown in Figure 12.3.

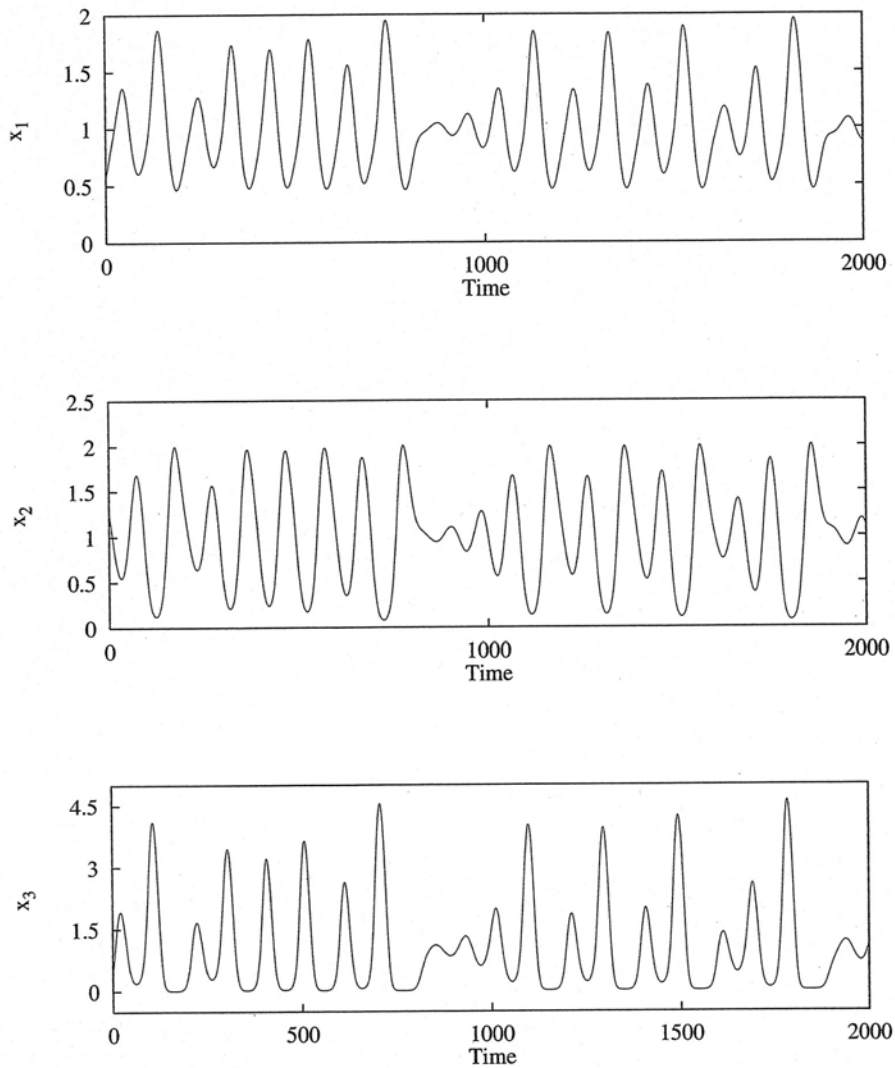


Figure 12.3 Population levels for the three-species Lotka-Volterra system

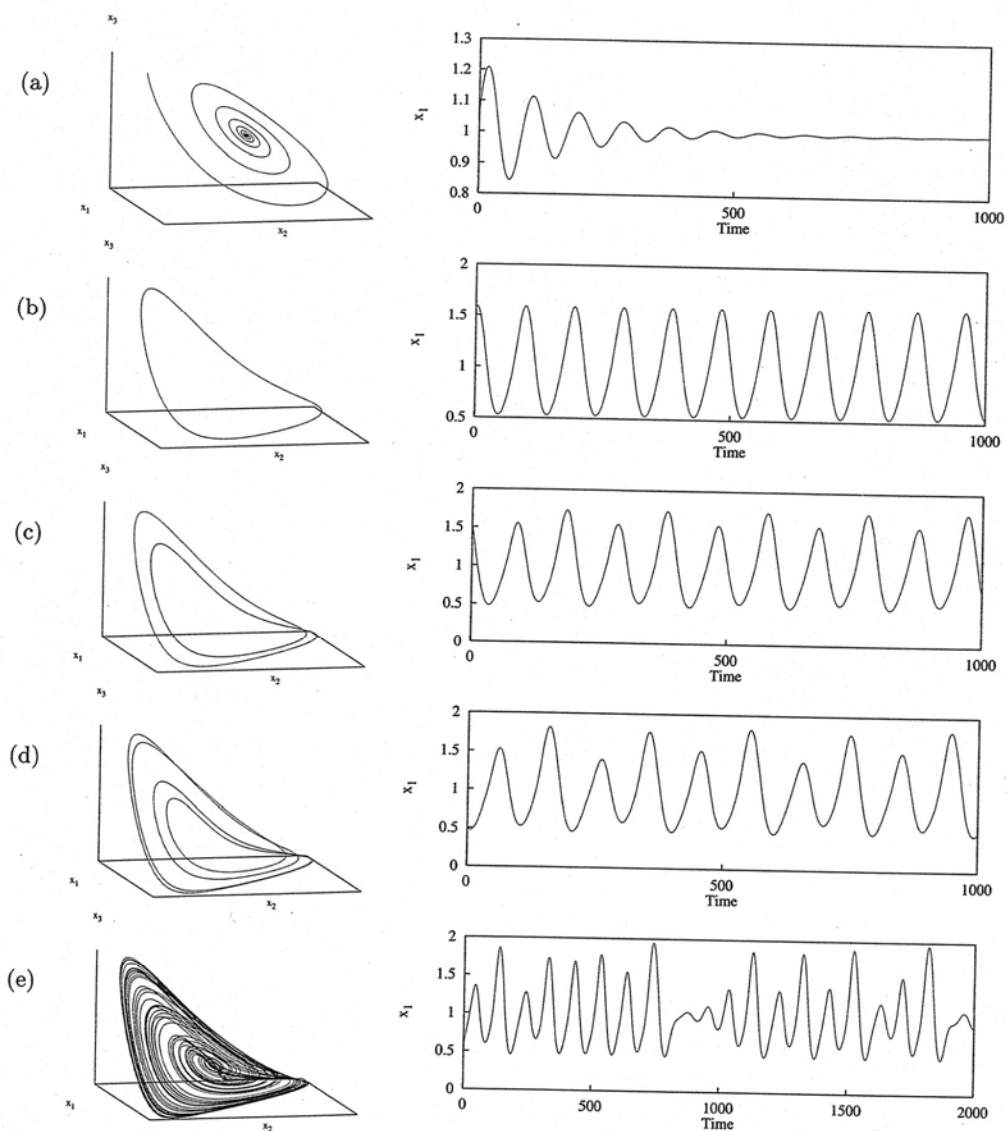


Figure 12.4 Period doublings in a three-species Lotka-Volterra system: phase space is on the left and x_1 is plotted on the right. (a) spiral fixed point, (b) simple periodic orbit, (c) period-2 orbit, (d) period-4 orbit, (e) chaos

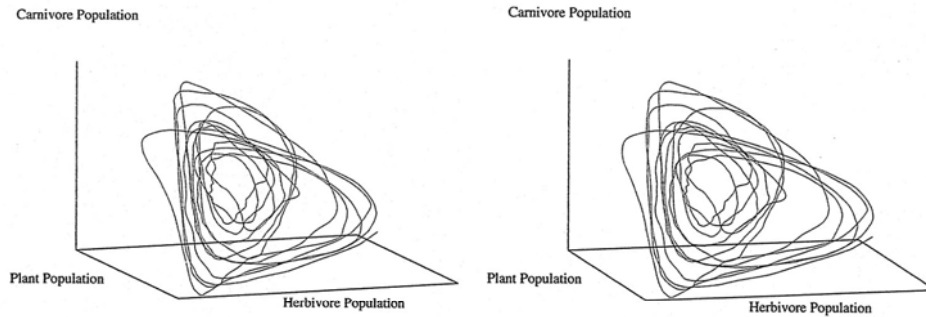


Figure 12.9 A dual-image stereogram of the attractor of the individual-based predator-prey system: To view, stare at the center of the two images and cross your eyes until the two images merge. Allow your eyes to relax so that they can refocus.

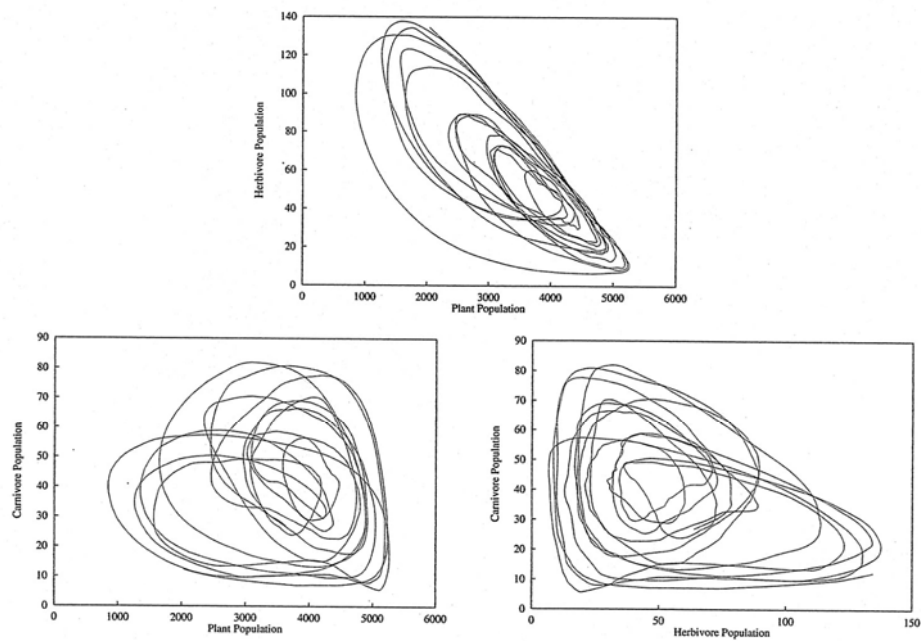


Figure 12.10 Population phase portraits for the individual-based predator-prey system

Vooluringi dünaamika

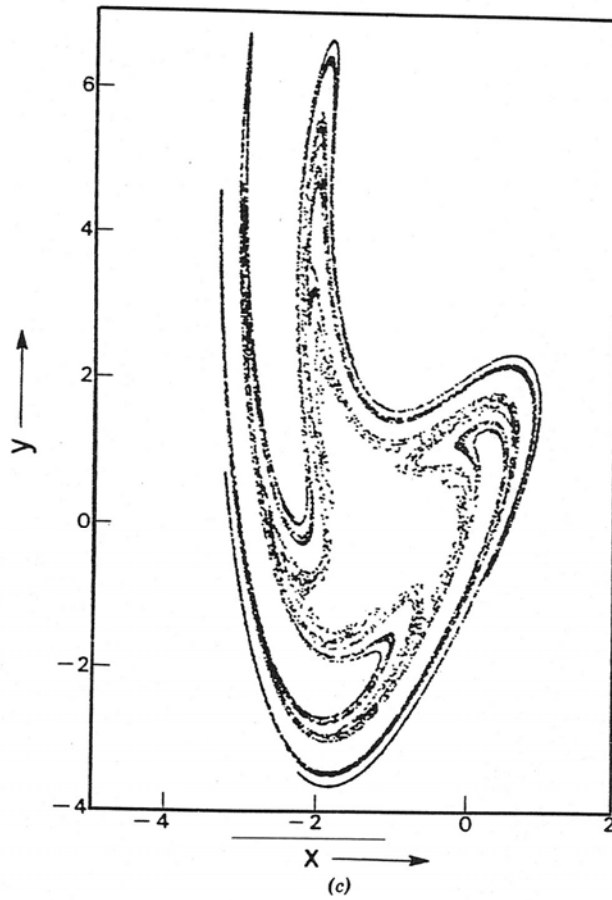
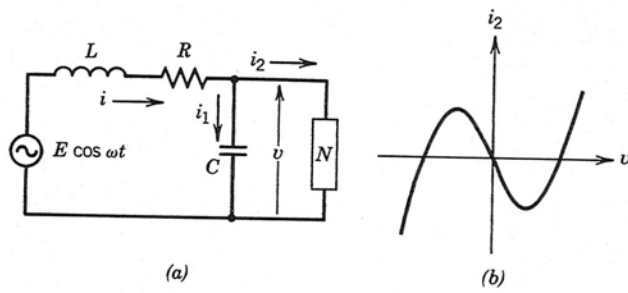


Figure 3-14 Poincaré map of chaotic analog computer simulation of a forced Van der Pol type circuit [from Ueda and Akamatsu (1981)].

Maa magnetväli

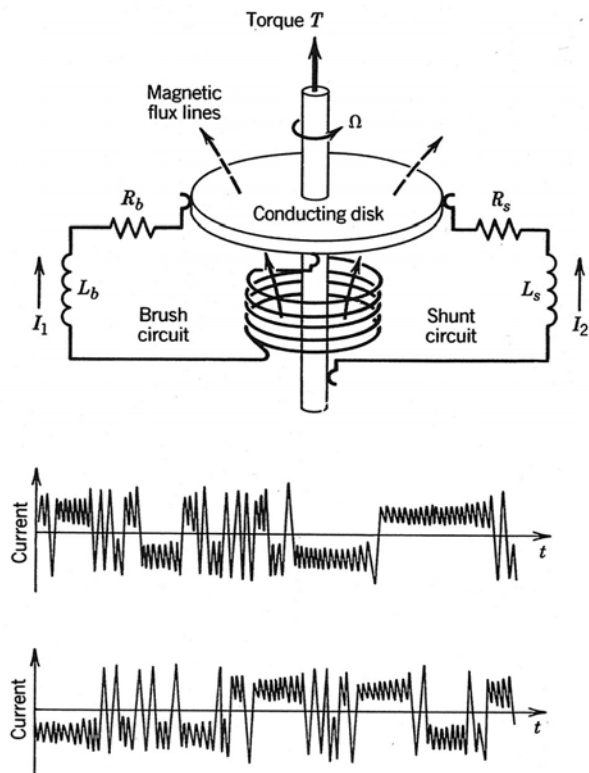


Figure 3-15 Top: Disk dynamo model of Robbins (1977) for reversals of the earth's magnetic field. Bottom: Chaotic current reversals from numerical solutions of disk dynamo equations (3-2.27).

Duffingi võrrand

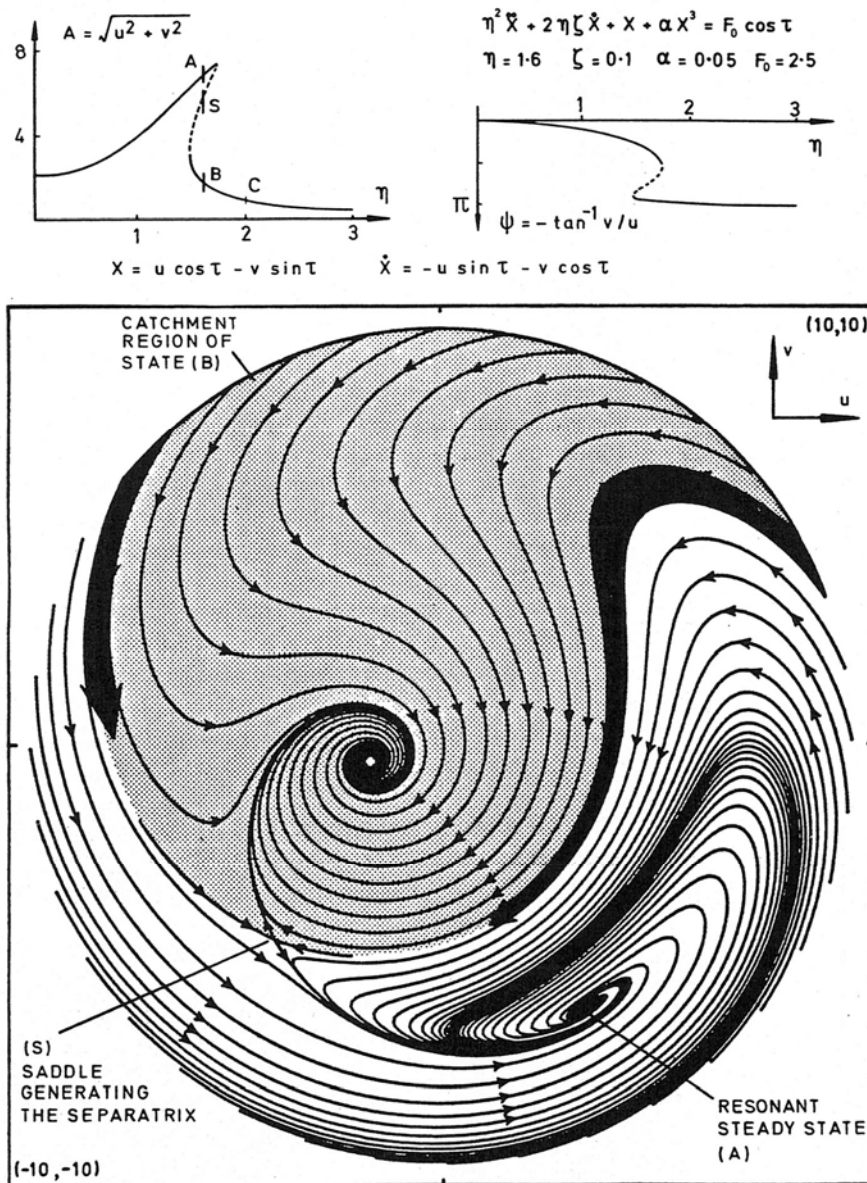


Figure 5.5 Phase portrait of smoothed variational equation of Duffing's equation in the Van der Pol plane. Above, the nonlinear resonance response and phase diagrams show a hysteresis regime in the fundamental resonance

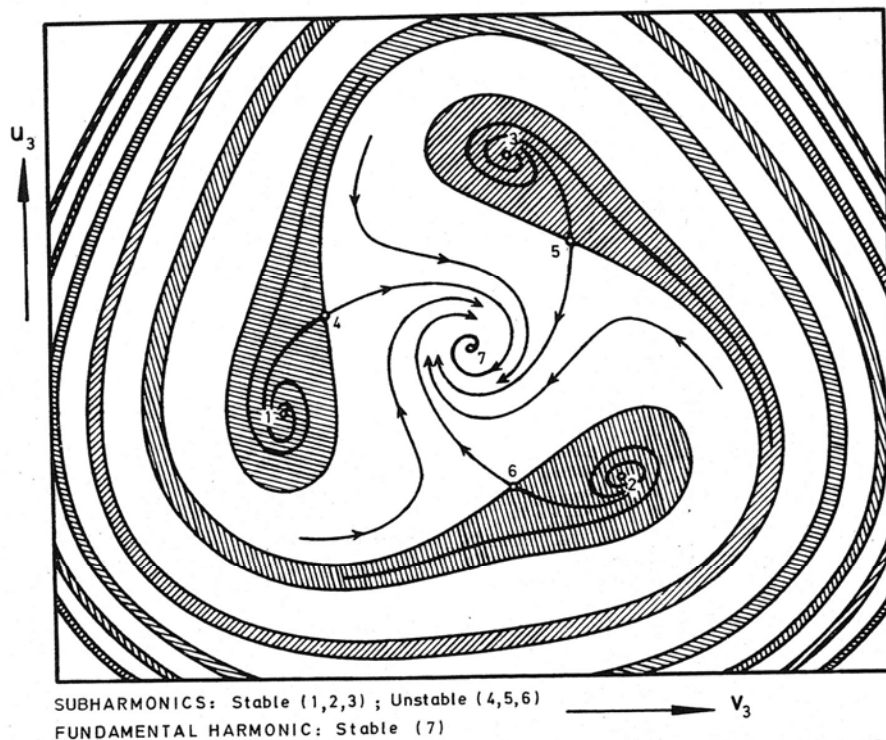


Figure 5.9 Phase portrait of smoothed variational equation of Duffing's equation in Van der Pol plane corresponding to subharmonics of order $n = 3$. *Reproduced by permission of McGraw-Hill Book Company from Hayashi, Nonlinear Oscillations in Physical Systems (1964).*

the domains of attraction, since it divides the whole (x, y) plane into its two catchment regions. Any initial point in one of the domains steps, under the repeated iterations of the mapping T , to the particular stable fixed point (2 or 3) that is located in the interior of that domain. The heavy invariant curve

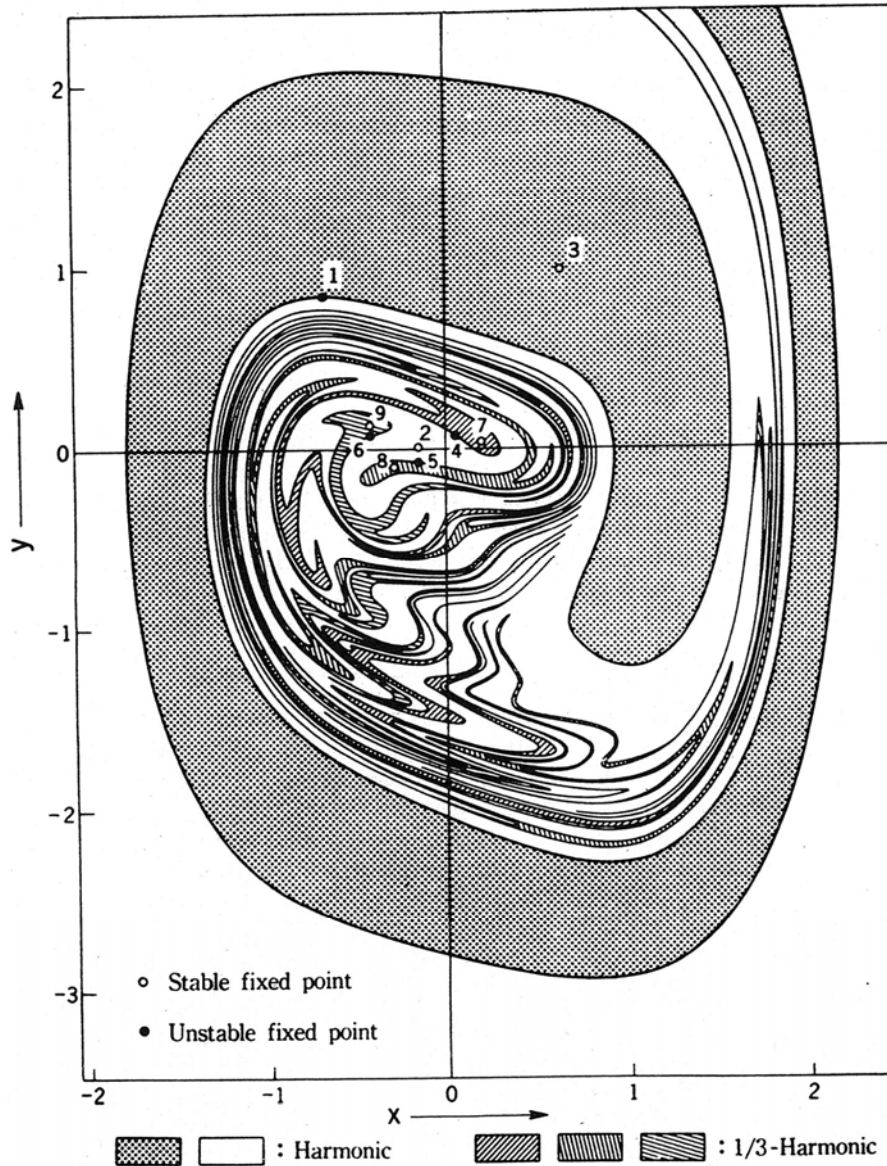
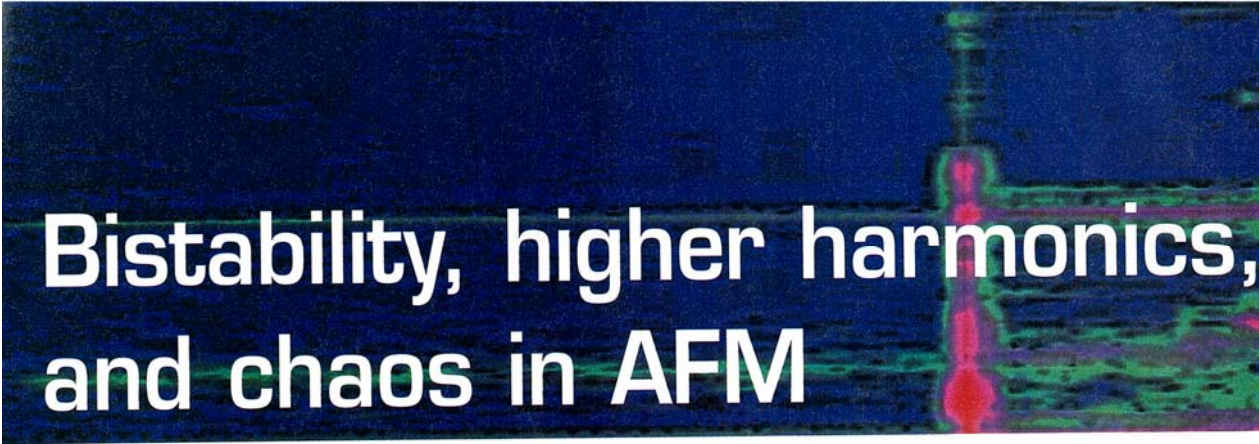


Figure 5.11 Domains of attraction for three harmonic and two coexisting subharmonics of order $n=3$ for Duffing's equation, as determined by Hayashi. *Reproduced by permission of McGraw-Hill Book Company from Hayashi, Nonlinear Oscillations in Physical Systems (1964)*



Bistability, higher harmonics, and chaos in AFM

A dynamic atomic force microscope sensitively probes surface properties with subnanometre lateral resolution. In the amplitude modulation mode, the force-sensing tip oscillates a few nanometres. The force sensor is a harmonic oscillator that interacts with a barrier, which can be described as a non-linear potential consisting of an attractive well and a repulsive wall. Further non-linearities may be introduced by adhesion, electrostatic or magnetic forces. Thus, the character of the non-linearity is intimately related to the material properties. This review highlights the non-linear dynamics in the amplitude modulation mode and how they enable and affect nanoscale material characterisation.

Robert W. Stark^{a,b}

^a Center of Smart Interfaces, TU Darmstadt, Petersenstr. 32, 64287 Darmstadt, Germany

^b FB Material- und Geowissenschaften, TU Darmstadt, Petersenstr. 32, 64287 Darmstadt, Germany

E-mail: stark@csi.tu-darmstadt.de

The atomic force microscope (AFM) is an instrument that has been optimised to measure and exert forces of less than a nanonewton with sub-nanometre spatial resolution. A well-defined experimental design together with mathematically understood operating modes are essential for high-resolution imaging and force sensing. Dynamic modes where the AFM tip only briefly interacts with the sample once per oscillation cycle are widely used for nanoscale surface characterisation^{1,2}. In what is called the tapping mode or amplitude modulation mode³, the AFM tip oscillates near its resonant frequency, and the variations of the amplitude are recorded (Fig. 1). The free oscillation amplitude A_0 , i.e., the amplitude measured far away from the influence of the specimen, is typically on the order of ten nanometres. Close to the specimen, the oscillation of the tip is influenced by the surface. This measurement mode has proven to be highly

valuable for material characterisation in an atmospheric or fluid environment^{4,5}. Thus, on one hand, non-linearity is the key to the high sensitivity of the AFM because the non-linear interaction strongly depends on the material. On the other hand, the non-linearities can disturb the harmonic oscillation of the AFM tip and lead to a rich dynamic response that affects the measurement. A thorough understanding of the non-linear dynamics thus helps to optimize sensitivity and resolution.

Single-mode approximation

To understand the origin of the non-linear dynamics, it is helpful to approximate the force sensor as a one-dimensional harmonic oscillator. In this approximation, we neglect higher eigenmodes of the cantilever beam such as higher flexural modes, torsional modes, or bending modes. This approximation allows us to predict basic features of the

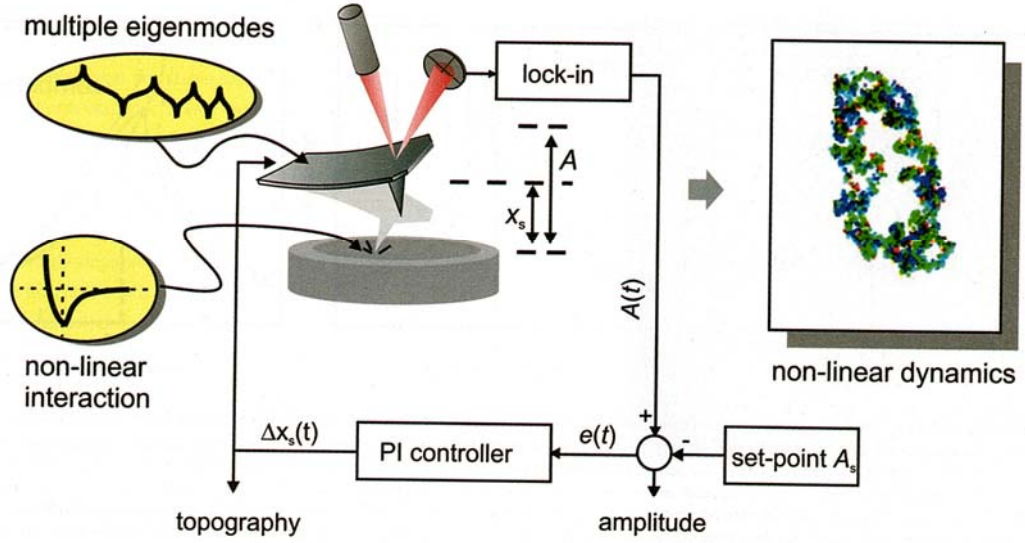


Fig. 1 The non-linear interaction between tip and sample together with the structural dynamics of the cantilever determine the system dynamics. In an amplitude-modulation AFM, the steady state oscillation amplitude $A(t)$ of the cantilever is measured with a lock-in technique and serves as the feedback signal³. The set-point ratio $A_s = A(t)/A_0$ serves as the guidance signal to maintain the gap between the cantilever and the surface x_s and thus to track the surface profile. Typical set-point ratios for imaging range from 50 % to 95 %. Usually, a proportional integral controller is used for feedback control, minimising the tracking error $e(t) = A_s - A(t)/A_0$ by readjusting the gap between tip and sample. The error signal image thus encodes variations of the amplitude $A(t)$ and is referred to as the 'amplitude' image. The 'topography' image is the output of the controller encoding perturbations caused by the surface morphology, noise, or the non-linear dynamics.

AFM dynamics such as the phase lag between driving force and system response⁶, the pressure in the contact area⁷, or the presence of more than one stable oscillatory state^{8,9}. Mathematically, the cantilever is characterised by its fundamental angular resonant frequency ω_0 , spring constant k , and quality factor Q . The quality factor $Q = 2\pi \Delta E/E$ accounts for the energy loss ΔE per cycle in the cantilever and in the surrounding medium and is related to the damping ratio γ by $Q = 1/(2\gamma)$. Typical quality factors are 50 to 500 in air and 1 to 10 in liquids. External forces due to driving or to the tip-sample interaction are summarised in the term $F(x,t)$. The state variables 'tip displacement' x and 'velocity' \dot{x} fully describe the dynamic system as follows:

$$\ddot{x}(t) + \frac{\omega_0}{Q} \dot{x}(t) + \omega_0^2 x(t) = \omega_0^2 F(x,t) / k \quad (1)$$

Eq. (1) can be rewritten in the state-space form

$$\dot{\mathbf{x}} = \mathbf{x} \begin{bmatrix} 0 & 1 \\ -\omega_0^2 & -\omega_0/Q \end{bmatrix} + \begin{bmatrix} 0 \\ 1 \end{bmatrix} \frac{\omega_0^2}{k} F(x,t) \quad (2)$$

\mathbf{A} \mathbf{b}

Here, we have introduced the state vector $\mathbf{x} = [x, \dot{x}]^T$. The system matrix \mathbf{A} accounts for the dynamics of the fundamental mode,

and the input vector \mathbf{b} describes the coupling of external forces to the oscillator. This approximation is good below and around the resonance¹⁰. It fails, however, to predict the high-frequency response, including transients or higher harmonics.

Surface forces, such as van der Waals or Pauli repulsion forces, determine the interaction between the tip and the sample. The distance between the two is $D = x_s + x$, where x is the deflection of the tip from the rest position and x_s is the distance between the undeflected tip and the surface. Interaction models usually combine the equations for the van der Waals forces ($D \geq a_0$) and for the repulsive regime ($D < a_0$). Mathematically, this leads to a piecewise smooth model because the force is only continuous for $F(x)$ but may show non-removable discontinuities for the higher order derivatives $\partial^n/\partial x^n F(x)$. This non-smoothness of the combined attractive and repulsive interaction model poses particular challenges for the mathematical analysis of the non-linear dynamics¹¹⁻¹⁵. As we will discuss later, it can affect the image quality because the transition between repulsive and attractive regime is very important for the dynamics of gentle repulsive imaging.

The Derjaguin-Muller-Toporov (DMT) model is a simple contact mechanics model for the interaction between a hard but compressible sphere and surface neglecting hysteretic adhesion forces¹⁶. The model describes, for example, the interaction between a silicon tip with a hard specimen, e.g., a metal, ceramics, or a semiconductor. The parameter a_0 , which corresponds to an interatomic distance, is used to achieve a continuous model for $F(x)$ ⁹. We thus obtain

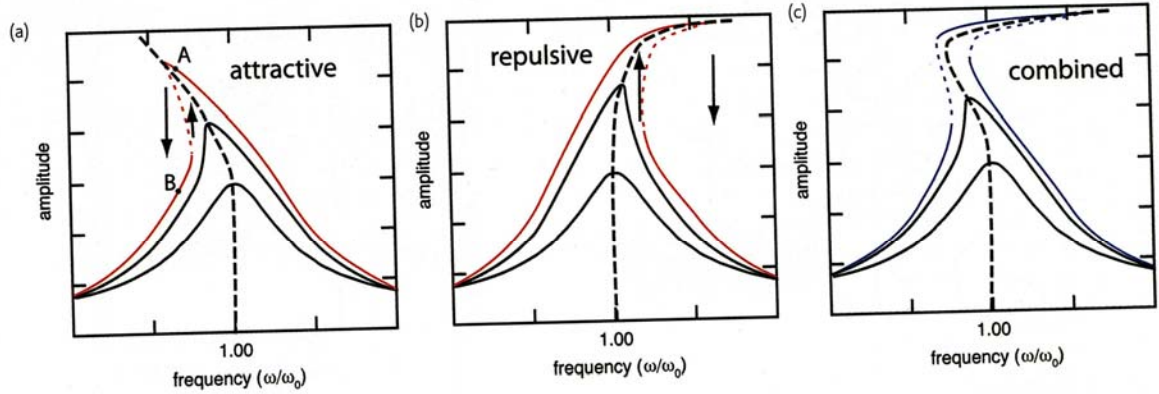


Fig. 2 Schematic illustration of bistability and hysteresis in a one dimensional non-linear system. (a) Purely attractive interaction. For small oscillations the tip does not 'see' the non-linearity and the resonance is very well approximated by the harmonic oscillator. For a stronger driving the resonance line in the amplitude vs. frequency plot is bent to the left side due to the attractive non-linear interaction. The resonance folds (red), i.e. there is more than one possible amplitude for a given frequency as for example in points A and B. This leads to bistability, where the system can oscillate either with a large or a small amplitude. Between the two stable solutions there is an unstable periodic solution (dotted line). The bistability is responsible for the hysteresis during a frequency sweep as indicated with the arrows. The black dashed line is the backbone line of the non-linear resonance. (b) The same plot for a purely repulsive interaction. (c) Non-linear resonance for a combined attractive-repulsive potential.

$$F(x) = \begin{cases} -HR / [6(x_s + x)^2] & D \geq a_0 \\ -HR / 6a_0^2 + \frac{4}{3} E^* \sqrt{R} (a_0 - x_s - x)^{3/2} & D < a_0 \end{cases} \quad (3)$$

The strength of the van der Waals interaction depends on the tip radius R and the Hamaker constant H , which depends on the materials of tip and sample and the medium between both. Both parameters determine the dynamics in the attractive domain. This implies that the quality of the tip is of paramount importance because the tip radius determines not only the lateral resolution but also the strength of the non-linear interaction. The mechanical interaction is summarised by an effective contact stiffness $E^* = [(1-\nu_t^2)/E_t + (1-\nu_s^2)/E_s]^{-1}$, where E_t and E_s are the

elastic moduli, and ν_t and ν_s are the Poisson ratios of tip and sample, respectively. A viscoelastic term

$$F_{vis}(x) = -\eta \dot{x} \sqrt{R} (a_0 - x_s - x_0) \quad (4)$$

may be introduced to account for energy loss during mechanical contact. More advanced models may also account for capillary forces, soft samples, or electrostatic or magnetic forces.

Bistability

One of the most prominent non-linear effects in amplitude-modulation AFM is the coexistence of several oscillatory states. The dynamic system may produce more than one stable solution under the given

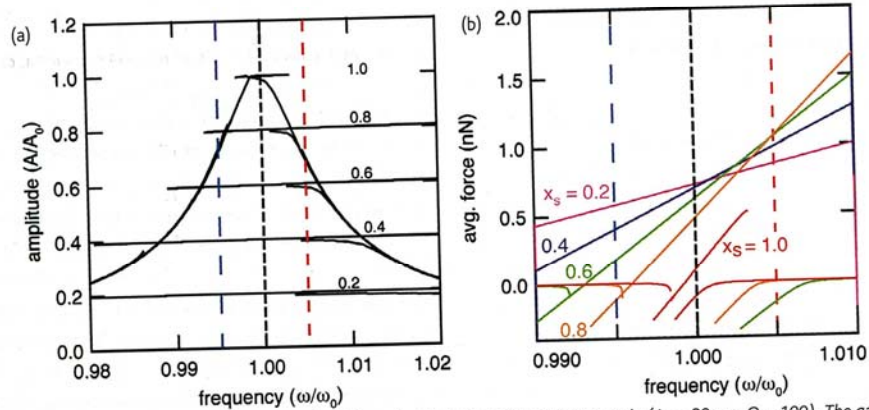


Fig. 3 (a) Non-linear amplitude response calculated for a typical silicon tip interacting with a glass sample ($A_0 = 20$ nm, $Q = 100$). The gap between tip and sample x_s was varied between 1.0 and 0.2. The dashed lines indicate typical driving frequencies. (b) Average interaction forces as a function of the driving frequency for different gaps x_s . The driving frequencies $\omega/\omega_0 = 0.995$, $\omega/\omega_0 = 1.000$, and $\omega/\omega_0 = 1.005$ are indicated by the vertical lines. For example, decreasing x_s for $\omega/\omega_0 = 0.995$ leads to increased forces. Reprinted with permission from¹⁰¹. © 2003, American Institute of Physics (modified).

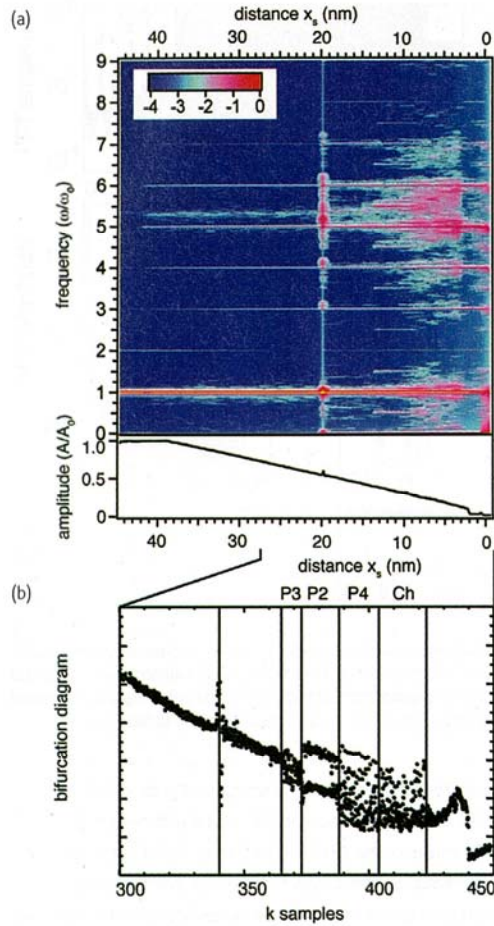


Fig. 6 Evolution from a periodic tip oscillation to chaos. (a) Spectrogram and oscillation amplitude and (b) bifurcation diagram obtained during an approach. The amplitude plot shows a monotonous decrease of the amplitude but does not capture the dynamics. The spectrogram above reveals that the driving frequency initially prevails in the spectrogram. At $x_s = 60$ nm, there is a sharp peak that accompanies the transition to the repulsive state. Approaching further at $x_s = 65$, subharmonics of the driving frequency occur that indicate period doubling. The bifurcation diagram also shows a period-4 regime, which is followed by an irregular system response. Reprinted with permission from⁵¹. © 2006, IOP Publishing Ltd (modified).

appropriate spring constant for a given material also the control circuitry of the AFM can be improved to suppress chaotic dynamics. To this end, various chaos control strategies have been suggested for implementation in future AFMs^{52–54}.

Higher modes and higher harmonics

Thus far, we have discussed non-linear phenomena on the basis of a single-degree-of-freedom model. The force sensor, however, is an extended micro-structure that is capable of various types of oscillation such as flexure, twisting or bending. Each oscillatory mode can be modelled as a harmonic oscillator with the respective resonant

frequency. If one adds important modes to the model such as for example, additional higher flexural modes, torsional or bending modes the accuracy of the model can be improved. Such multiple-degrees-of-freedom (MDOF) models are needed in particular, if the cantilever is excited at more than one resonant frequency. Such an excitation of a higher eigenmode can occur, for example, due to the generation of higher frequencies by the non-linear dynamics or due to active driving at multiple frequencies. Mathematically, MDOF models can be derived with analytical methods⁵⁵, finite element modelling^{56–60}, or finite difference analysis⁶¹. Recently, Raman and co-workers published a freely available numerical simulation environment that allows microscopists to explore the consequences of the non-linear dynamics in AFM with MDOF models¹¹.

In the state-space model we extend Eq. (2) and treat N eigenmodes of the model as independent harmonic oscillators^{62,63}

$$\begin{aligned}\dot{\mathbf{x}} &= \mathbf{A}\mathbf{x} + \mathbf{b}u \\ \mathbf{y} &= \mathbf{C}\mathbf{x}\end{aligned}\quad (5)$$

The model implies that we assume that the AFM sensor is a linear system that does not change with time. Each eigenmode included in the model is treated as an individual harmonic oscillator with

$$\mathbf{x}_n = \begin{bmatrix} x_n \\ \dot{x}_n \end{bmatrix}, \mathbf{A}_n = \begin{bmatrix} 0 & 1 \\ -\omega_n^2 & -\omega_n/Q_n \end{bmatrix}, \mathbf{b}_n = \begin{bmatrix} 0 \\ \varphi_n \end{bmatrix}. \quad (6)$$

The quantities $\mathbf{x}_n = [x_n, \dot{x}_n]^T$ and \mathbf{A}_n , with ω_n , Q_n and \mathbf{b}_n , now account for the respective quantity of the n -th mode. The parameters φ_n define the coupling between the external force and the n -th eigenmode. The entire system can be constructed with these subsystems

$$\begin{bmatrix} \dot{x}_1 \\ \dot{x}_2 \\ \vdots \\ \dot{x}_N \end{bmatrix} = \begin{bmatrix} \mathbf{A}_1 & 0 & \cdots & 0 \\ 0 & \mathbf{A}_2 & \cdots & 0 \\ \vdots & \vdots & \ddots & \vdots \\ 0 & 0 & & \mathbf{A}_N \end{bmatrix} \begin{bmatrix} x_1 \\ x_2 \\ \vdots \\ x_N \end{bmatrix} + \begin{bmatrix} \mathbf{b}_1 \\ \mathbf{b}_2 \\ \vdots \\ \mathbf{b}_N \end{bmatrix} u. \quad (7)$$

The new state-vector $\mathbf{x} = (x_1, x_2, \dots) = (x_{n=1}, \partial_t x_{n=1}, \dots)$ contains the displacements and velocities of the N eigenmodes. The system \mathbf{A} is now a $2N \times 2N$ matrix, and \mathbf{b} is now a $2N$ vector. The scalar $u = F(x, t)$ is still the force input that accounts for external forces and the non-linear interaction. To calculate the tip position and velocity, the contributions of the N eigenmodes have to be added^{63,64}. With such a model the vibration of the cantilever can be modelled. The non-linear interaction is treated as an output feedback, where the tip deflection is calculated by the dynamic system (Eq. (5)). The output \mathbf{y} is transformed into a force by the nonlinearity. The resulting interaction force is then fed back to the tip^{62,63,65,66}. In the following we assume only flexural oscillations of the first N flexural modes.

MDOF models are needed, for example, to correctly predict the spectrum of higher harmonics of the cantilever response. In this

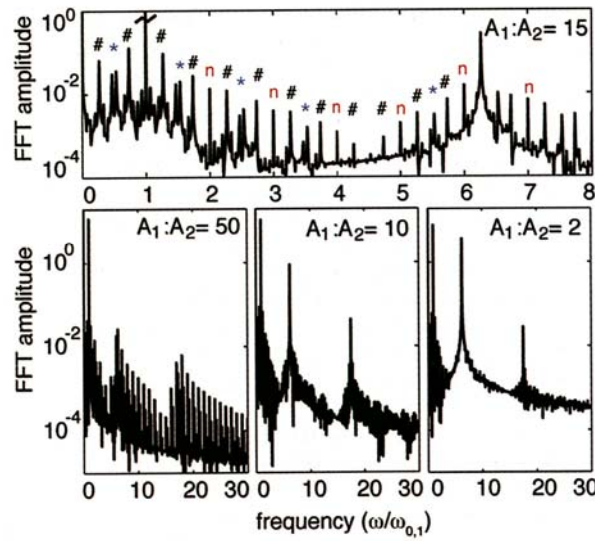


Fig. 8 Spectra predicted for dual-frequency excitation for an amplitude set-point of $A_2/A_{0,1} = 80\%$. For a small second-eigenmode oscillation, the harmonics of the driving frequency (n) and intermodulation products are well defined. Frequencies following the rule $\omega = \pm \omega_2 \pm n \omega_1$ are marked by '#' and those according to $\omega = \pm 2\omega_2 \pm n \omega_1$ by '*'. Because the harmonics n are very prominent in the spectrum, intermodulation products of very high order also occur. For large second-eigenmode contributions ($A_1:A_2 = 10$), the peaks broaden due to a quasi-periodic oscillation, where the instantaneous partial frequencies are only nearly harmonic frequencies. At $A_1:A_2 = 2$, the instantaneous frequencies of the harmonic peaks are severely detuned, and the distinct harmonic and intermodulation peaks vanish, indicating that the trajectory is no longer periodic. Reprinted with permission from¹². © 2009, American Institute of Physics.

calculations predict that at large second-mode amplitudes, even quasi-periodic or chaotic dynamics may occur, where the tip repulsively hits the specimen quasiperiodically or even aperiodically¹².

Thus far, we have discussed weakly damped systems as they occur for an AFM operating in air. In a liquid environment, the damping is much stronger. Typical quality factors of soft cantilevers are then on the order of $Q = 1$ to 5 , which means that the oscillator 'forgets' its history within very few oscillations. The actual impact in each oscillatory cycle is much more important for the dynamics than the impacts that occurred before, and thus non-linear transients become relevant to the dynamics. A highly important phenomenon is the momentary excitation of a higher eigenmode⁹⁶⁻⁹⁸. As illustrated in Fig. 9, the tip impacts on the sample surface at the lower turning point of each oscillation of the fundamental mode. The impact forces help to restore the motion of the fundamental mode but also excite the second eigenmode. As the resonance of the higher eigenmode is much larger than that of the fundamental, the higher-eigenmode oscillation has nearly rung down when the next impact occurs. Thus, the entire energy that was transferred into the second eigenmode has been dissipated. The transient excitation and ringing out of the second eigenmode contribute to the overall dynamics and represent

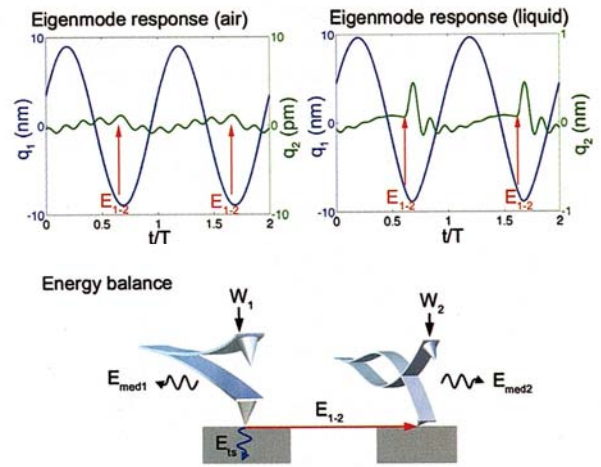


Fig. 9 Momentary excitation of the second eigenmode in a liquid environment. At the lower turning point of the oscillation (amplitude q_1), the tip hits the sample, which leads to the excitation of the second eigenmode with amplitude q_2 . In air only small but sustained oscillations are induced. In liquids, however, the coupling is stronger and the ringing of the second mode is dampened within a few oscillations. This mechanism transfers energy E_{1-2} from the first to the second eigenmode and is an important channel for energy dissipation of the first mode in addition to dissipation in the medium E_{med} and the sample E_{Ls} . Reprinted with permission from⁹⁹.

an important channel for energy transfer from the fundamental mode to a higher eigenmode, which also determines the phase image of the fundamental mode⁹⁹. Because the strength of the repulsive force depends on the material properties of the specimen, the momentary excitation of a higher eigenmode can readily be used for compositional mapping in a fluid environment⁹⁷. To achieve an accurate image of the specimen, the signal of the fundamental mode can be isolated by adjusting the target of the detection laser to the antinode of the second eigenmode at about one half of the cantilever length¹⁰⁰.

Outlook

Various methods are now available to probe the non-linearity of the contact between the tip and the sample. This non-linearity is determined by the details of the interaction and thus encodes the material properties of tip and sample. A mathematical understanding of the non-linear dynamics helps us to solve the inverse problem, i.e. to estimate the material properties from the system response. Compositional mapping can be achieved with very high resolution and sensitivity, and even the characterisation of soft matter, such as biomolecules, has become possible with very high resolution. The quantitative measurement of material properties, however, still remains a challenge. It is still very difficult to precisely calibrate the tip radius, which is one important parameter determining the mechanical non-linearity [Eq. (3)]. Here durable AFM tips with well-defined radii will help to push the limits further.

Galaktikate jaotus

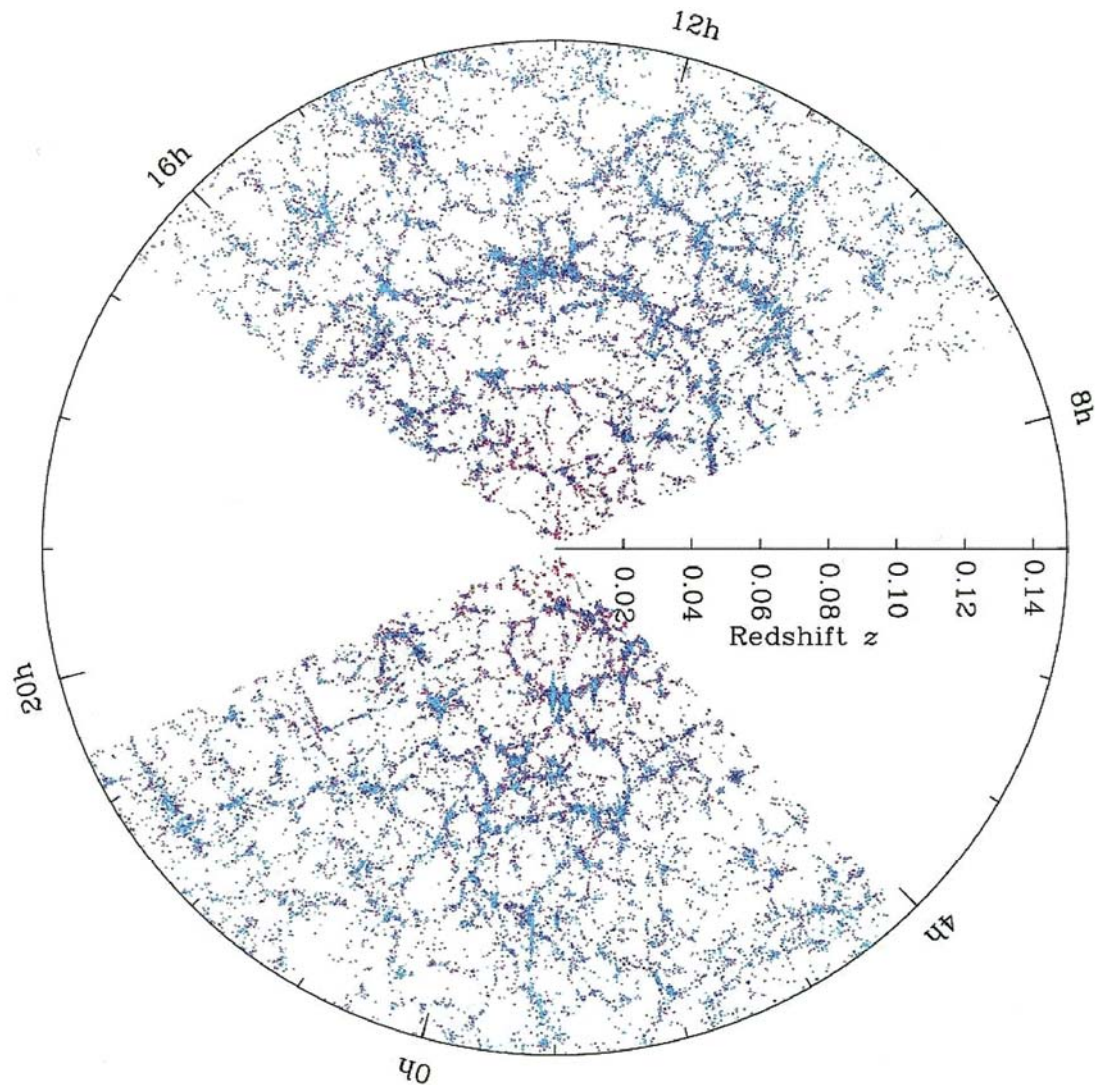


Figure 2: tranche d'Univers, où chaque point est une galaxie, dont la distance est connue par son décalage vers le rouge z . Notre galaxie est au sommet des deux cônes. (crédit Sloan Digital Sky Survey, <http://www.sdss.org/>).

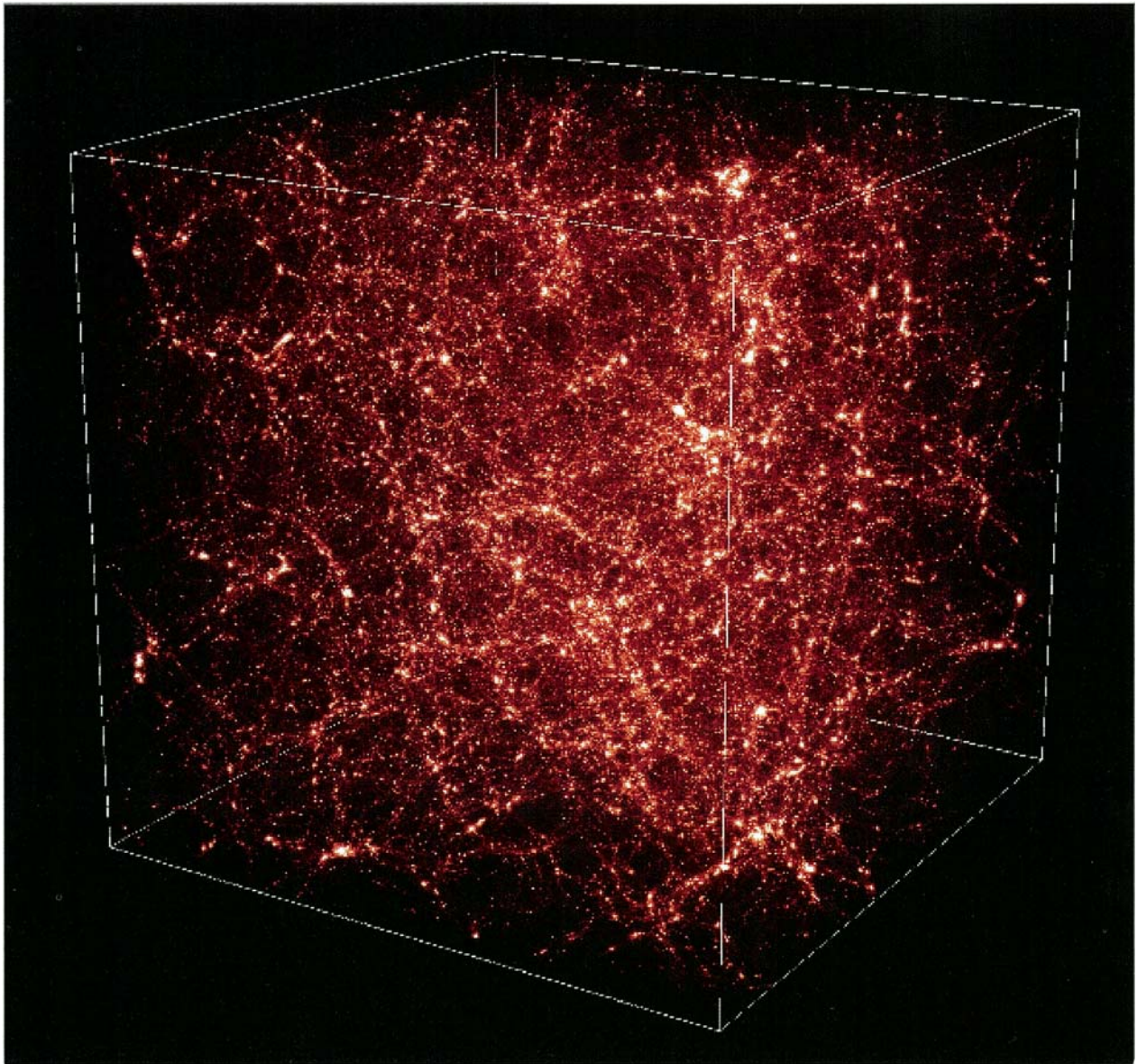


Figure 1 : simulations numériques de la formation des structures (crédit Projet Horizon, <http://www.projet-horizon.fr/>). Le projet Horizon rassemble depuis 2005 les principaux groupes de simulations extra-galactiques en France, soit une vingtaine de chercheurs, afin de progresser de façon significative dans le problème de la formation des galaxies dans un contexte cosmologique. Les plus grosses simulations au niveau international ont été effectuées dans ce cadre, comprenant non seulement la matière noire, mais l'hydrodynamique du gaz, la formation des grandes structures, des premières étoiles, etc. Les plus ambitieuses recouvrent une région du ciel comprenant tout l'Univers observable aujourd'hui, jusqu'à l'horizon cosmique (ou remontée dans le temps/espace de 13,7 milliards d'années-lumière), d'où le nom du projet.

Complicated billiard tables and maps

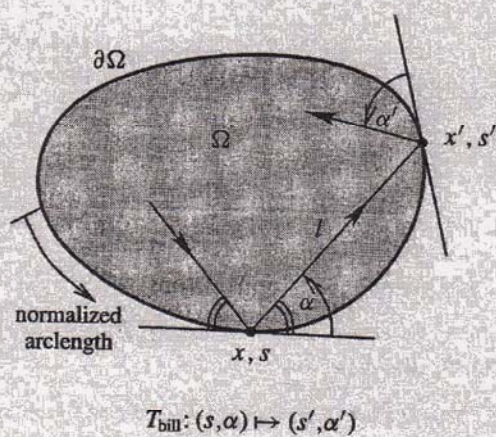
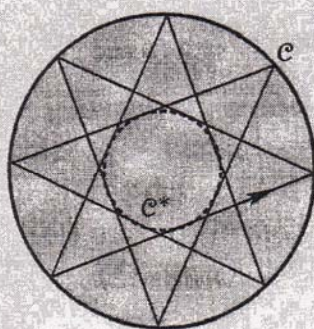
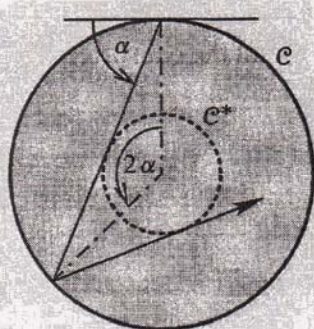
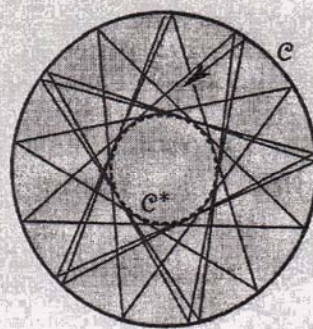


Figure 2.21. The billiard map



$$\alpha/\pi = 3/8 \in \mathbb{Q}$$



$$\alpha/\pi \notin \mathbb{Q}$$

Figure 2.22. Each circle concentric to \mathcal{C} is a caustic for the circular billiard.

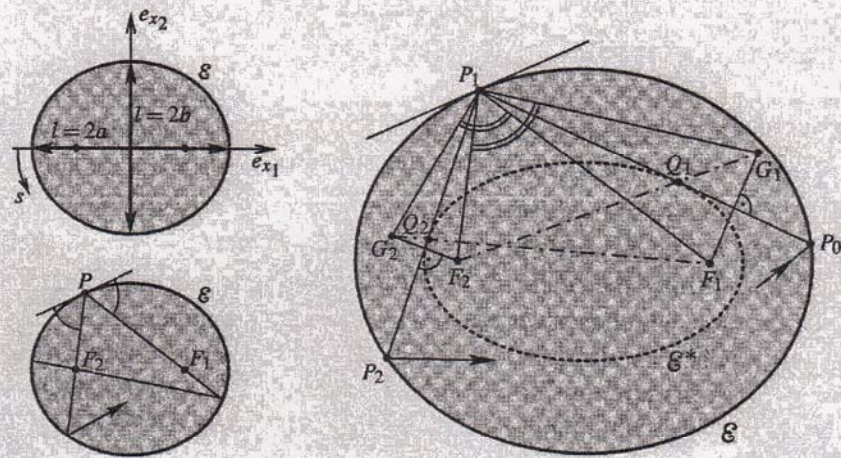


Figure 2.23. Two-periodic trajectories (upper left) and geometric details of the caustic construction for the elliptic billiard

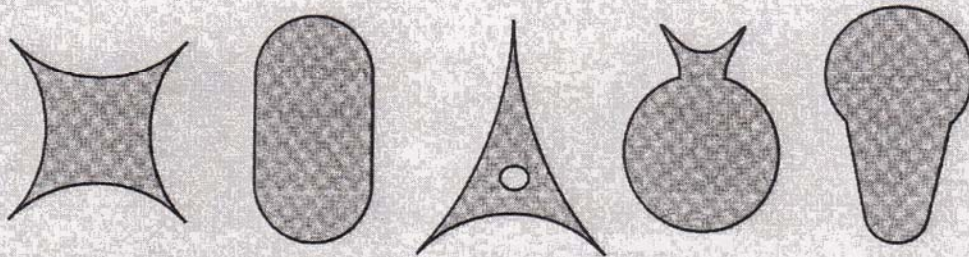


Figure 3.11. For these tables the associated billiard map T_{bill} is ergodic.

Predicting the outcome of roulette

Michael Small^{1,2,a)} and Chi Kong Tse²

¹School of Mathematics and Statistics, The University of Western Australia, Perth, Australia

²Department of Electronic and Information Engineering, Hong Kong Polytechnic University, Hong Kong

(Received 30 April 2012; accepted 4 September 2012; published online 26 September 2012)

There have been several popular reports of various groups exploiting the deterministic nature of the game of roulette for profit. Moreover, through its history, the inherent determinism in the game of roulette has attracted the attention of many luminaries of chaos theory. In this paper, we provide a short review of that history and then set out to determine to what extent that determinism can really be exploited for profit. To do this, we provide a very simple model for the motion of a roulette wheel and ball and demonstrate that knowledge of initial position, velocity, and acceleration is sufficient to predict the outcome with adequate certainty to achieve a positive expected return. We describe two physically realizable systems to obtain this knowledge both *incognito* and *in situ*. The first system relies only on a mechanical count of rotation of the ball and the wheel to measure the relevant parameters. By applying these techniques to a standard casino-grade European roulette wheel, we demonstrate an expected return of at least 18%, well above the -2.7% expected of a random bet. With a more sophisticated, albeit more intrusive, system (mounting a digital camera above the wheel), we demonstrate a range of systematic and statistically significant biases which can be exploited to provide an improved guess of the outcome. Finally, our analysis demonstrates that even a very slight slant in the roulette table leads to a very pronounced bias which could be further exploited to substantially enhance returns. © 2012 American Institute of Physics. [<http://dx.doi.org/10.1063/1.4753920>]

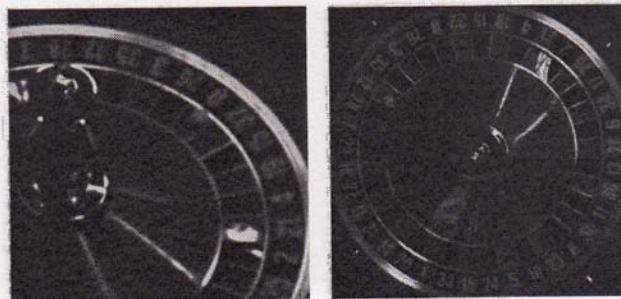


FIG. 1. The European roulette wheel. In the left panel, one can see a portion of the rotating roulette wheel and surrounding fixed track. The ball has come to rest in the (green) 0 pocket. Although the motion of the wheel and the ball (in the outer track) are simple and linear, one can see the addition of several metal deflectors on the *stator* (that is, the fixed frame on which the rotating wheel sits). The sharp *friction* between pockets also introduce strong nonlinearity as the ball slows and bounces between pockets. The panel on the right depicts the arrangement of the number 0 to 36 and the coloring red (lighter) and black (darker).

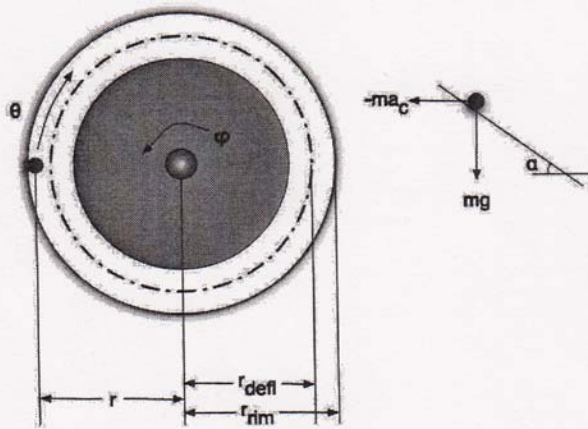


FIG. 2. The dynamic model of ball and wheel. On the left, we show a top view of the roulette wheel (shaded region) and the stator (outer circles). The ball is moving on the stator with instantaneous position (r, θ) while the wheel is rotating with angular velocity ϕ (note that the direction of the arrows here are for illustration only, the analysis in the text assume the same convention, clockwise positive, for both ball and wheel). The deflectors on the stator are modelled as a circle, concentric with the wheel, of radius r_{defl} . On the right, we show a cross section and examination of the forces acting on the ball in the incline plane of the stator. The angle α is the incline of the stator, m is the mass of the ball, a_c is the radial acceleration of the ball, and g is gravity.

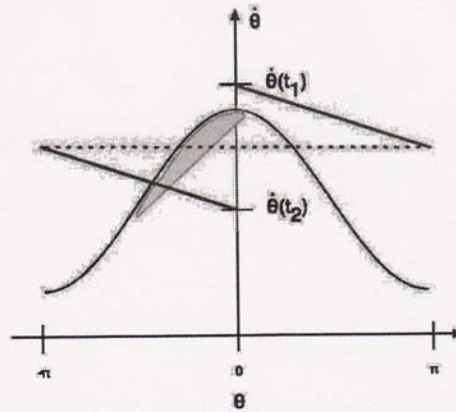


FIG. 3. The case of the crooked table. The blue curve denotes the stability criterion (6), while the red solid line is the (approximate) trajectory of the ball, with $\theta(t_1) + 2\pi = \theta(t_2)$ indicating two successive times of complete revolutions. The point at which the ball leaves the rim will therefore be the first intersection of this stability criterion and the trajectory. This will necessarily be in the region to the left of the point at which the ball's trajectory is tangent to Eq. (6), and this is highlighted in the figure as a green solid. Typically a crooked table will only be slightly crooked and hence this region will be close to $\theta = 0$ but biased toward the approaching ball. The width of that region, depends on $\theta(t_1) - \theta(t_2)$, which in turn can be determined from Eq. (6).

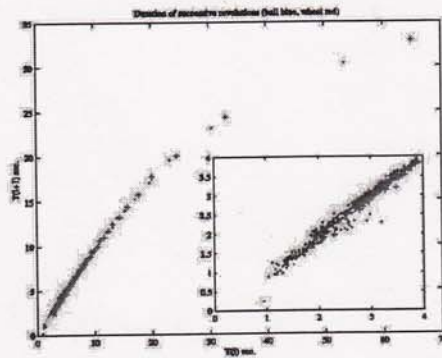


FIG. 4. Hand-measurement of ball and wheel velocity for prediction. From two spins of the wheel, and 20 successive spins of the ball we logged the time (in seconds) $T(i)$ for successive passes past a given point ($T(i)$ against $T(i+1)$). The measurements $T(i)$ and $T(i+1)$ are the timings of successive revolutions—direct measurements of the angular velocity observed over one complete rotation. To provide the simplest and most direct indication that handheld measurements of this quantity are accurate, we indicate in this figure a deterministic relationship between these quantities. From this relationship, one can determine the angular deceleration. The red (slightly higher) points depict these times for the wheel, the blue (lower) points are for the ball. A single trial of both ball and wheel is randomly highlighted with crosses (superimposed). The inset is an enlargement of the detail in the lower left corner. Both the noise and the determinism of this method are evident. In particular, the wheel velocity is relatively easy to calculate and decays slowly, in contrast the ball decays faster and is more difficult to measure.

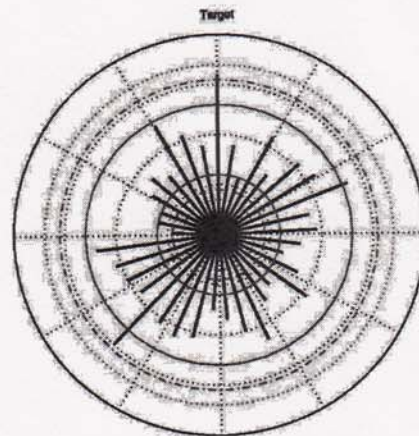


FIG. 5. Predicting roulette. The plot depicts the results of 700 trials of our automated image recognition software used to predict the outcome of independent spins of a roulette wheel. What we plot here is a histogram in polar coordinates of the difference between the predicted and the actual outcome (the "Target" location, at the 12 o'clock position in this diagram, indicating that the prediction was correct). The length of each of the 37 black bars denote the frequency with which predicted and actual outcome differed by exactly the corresponding angle. Dotted, dotted-dashed, and solid (red) lines depict the corresponding 99.9%, 99%, and 90% confidence intervals using the corresponding two-tailed binomial distribution. Motion forward (i.e., ball continues to move in the same direction) is clockwise, motion backwards is anti-clockwise. From the 37 possible results, there are 2 instances outside the 99% confidence interval. There are 7 instances outside the 90% confidence interval.

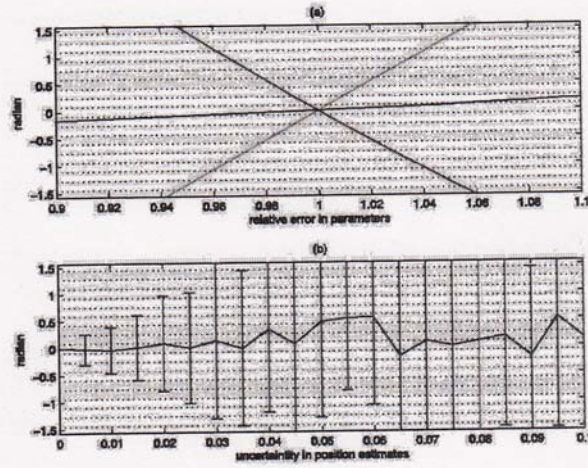


FIG. 6. Parameter uncertainty. We explore the effect of error in the model parameters on the outcome by varying the three physical parameters of the wheel (a) and introducing uncertainty in the measurement of timing events used to obtain estimates of velocity and deceleration (b). In (a), we depict the effect of perturbing the estimated values of α (green—affine, increasing steeply) r_{max} (red—affine, decreasing) and r_{eff} (blue—affine and increasing slowly) from 90% to 110% of the true value. In (b), we add Gaussian noise of magnitude between 0.5% and 10% the variance of the true measurements to initial estimates of all positions and velocities. Horizontal dotted lines in both plots depict error corresponding to one whole pocket in the wheel. The vertical axis is in radians and covers $\pm \frac{1}{2}$ half the wheel. In the upper panel, least variation in outcome is observed with errors in estimation of r_{eff} .